RICE UNIVERSITY

Patient-Specific Computer Modeling of Blood Flow in Cerebral Arteries With Aneurysm and Stent

by

Kathleen M. Schjodt, 2nd Lt, USAF

A Thesis Submitted
in Partial Fulfillment of the
Requirements for the Degree

Master of Science

Approved, Thesis Committee:

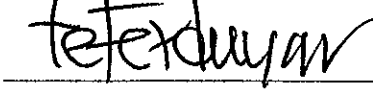

T. E. Tezduyar, Chair
Professor of Mechanical Engineering and
Materials Science

J. E. Akin
Professor of Mechanical Engineering and
Materials Science and Professor of
Computational and Applied Mathematics

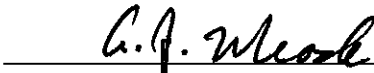

A. J. Meade
Professor of Mechanical Engineering and
Materials Science

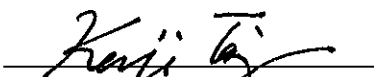

K. Takizawa
Associate Professor in Department of
Modern Mechanical Engineering and
Waseda Institute for Advanced Study
Waseda University, Tokyo, Japan

Houston, Texas
April 2012

The views expressed in this thesis are those of the author and do not reflect the official policy or position of the United States Air Force, Department of Defense, or the U. S. Government.

Abstract

Patient-Specific Computer Modeling of Blood Flow in Cerebral Arteries With Aneurysm and Stent

by

Kathleen M. Schjodt

This thesis focuses on special arterial fluid mechanics techniques developed for patient-specific computer modeling of blood flow in cerebral arteries with aneurysm and stent. These techniques are used in conjunction with the core computational technique, which is the space-time version of the variational multiscale (VMS) method and is called "DST/SST-VMST." The special techniques include using NURBS for the spatial representation of the surface over which the stent mesh is built, mesh generation techniques for both the finite- and zero-thickness representations of the stent, techniques for generating refined layers of mesh near the arterial and stent surfaces, and models for representing double stent. We compute the unsteady flow patterns in the aneurysm and investigate how those patterns are influenced by the presence of single and double stents. We also compare the flow patterns obtained with the finite- and zero-thickness representations of the stent.

Acknowledgments

To begin, I would like to thank Dr. Tayfun Tezduyar for affording me the opportunity to study with T★AFSM at Rice University. The experience I gained while participating in a group at the forefront of computational flow modeling was invaluable. I would also like to offer much thanks to Dr. Kenji Takizawa. He is one of the most intelligent people I have ever met and his work ethic is inspiring. It was a pleasure to work with him.

Much appreciation is owed to the members of my thesis committee. To Dr. Tezduyar, Dr. Akin, Dr. Meade, and Dr. Takizawa, thank you for your time and input. I would like to thank the members of T★AFSM with whom I had the privilege of working with: Anthony Puntel, Darren Montes, Nikolay Kostov, Matthew Fritze, Tyler Brummer, Tim Spielman, Tracee Curlett, Brad Henicke, Joe Boben, and Spenser McIntyre.

Thank you to my parents, Steve and Colleen, and my brother, Danny, for always supporting me in my education and career. I would not be where I am today without your love and encouragement. To my extended family, thank you for always being there for me. I would also like to thank my new family, Bud, Jeannine, Jarad, and Kayla, for your love and support over the past few years. Thank you for welcoming me into your home and family.

Most importantly, thank you to my amazing husband, Adam, for loving and supporting me as I worked toward this goal. You sacrificed much during the last two

years and I thank you for your patience and encouragement. You are truly my best friend and I would not have done so well without your unwavering love.

This work was supported in part by a seed grant from the Gulf Coast Center for Computational Cancer Research funded by John & Ann Doerr Fund for Computational Biomedicine. It was also supported in part by the Program to Disseminate Tenure Tracking System, Ministry of Education, Culture, Sports, Science and Technology, Japan. Supercomputing resources were provided in part by the Rice Computational Research Cluster funded by NSF Grant CNS-0821727. We thank Dr. Ryo Torii (Imperial College) for the inflow velocity waveform used in the computations. Dr. Peng R. Chen (University of Texas Medical School at Houston) provided the stent sample.

Contents

List of Figures

List of Tables

Chapter 1

Introduction

The complex patterns of pulsatile blood flow in cerebral arteries along with the elasticity of the arterial wall has motivated development of extensive fluid mechanics modeling techniques to further understand the multifaceted phenomenon. Much work focused on patient-specific modeling of cerebral arteries with aneurysm and capturing the dependence of the arterial wall deformation and blood flow on each other using fluid-structure interaction (FSI) computations (see, for example, [46, 47, 48, 4, 40, 49, 50, 3, 41, 51, 2, 15, 19, 42, 52, 6, 7, 28, 45, 30, 53, 54, 9, 25, 8, 5, 20, 10, 12, 11, 31, 17, 55, 43, 14, 27, 18, 26]). The Team for Advanced Flow Simulation and Modeling (T★AFSM) at Rice University (Houston) and Waseda University (Tokyo) has developed robust computational mechanics techniques to target FSI problems and numerous special techniques to specifically handle arterial fluid mechanics. A few recent studies have involved comparing the fluid and structural mechanics of ruptured and unruptured aneurysms [27], as well as simulating occlusion of the aneurysm through virtual "surgery" [31]. The emergence of new medical techniques using a stent to treat and prevent aneurysms from rupturing motivated the following work, which computes the fluid mechanics in arterial geometries with aneurysm and stent.

1.1 Motivation

Cerebral aneurysms develop when a weakened area of an arterial wall enlarges or "balloons" out forming either a saccular or fusiform shape. Saccular shaped aneurysms vary in size and shape but all have a defined neck from the parent artery to the aneurysm and are the focus of the following study. Aneurysms develop primarily at the circle of Willis, the circular arterial network located at the base of the brain, which performs the vital function of controlling blood supply to the brain. A ruptured aneurysm in this region causes a subarachnoid hemorrhage (SAH), characterized by blood leaking into the space surrounding the brain, frequently resulting in severe brain damage or death. Preventing and managing ruptures and the subsequent SAH requires detecting and treating aneurysms before rupture [13, 24].

An estimated 2–5% of the population has a cerebral aneurysm with 0.5–3% rupturing each year, resulting in an hemorrhagic stroke. Stroke ranks fourth among leading causes of death. Strokes caused by SAH only comprise approximately 3% of all strokes but exhibit devastating effects with a mortality rate of 40% and severe morbidity in 30% of all cases. Unfortunately, treatment of an aneurysm after rupture, although necessary to prevent further damage and death, does not reverse damage already caused by the bleeding. Less than 30% of patients with a ruptured aneurysm return to normal activities with little to no disability. The debilitating effects stimulated by a ruptured aneurysm accentuates the need for detection and treatment of aneurysms before rupture. Various methods of modern imaging diagnostics, including 3D Rotational Angiography (3DRA), enable the detection of an aneurysm providing details on location, size, and feasibility of preventive treatment. Surgical clipping and endovascular treatments are the primary treatment methods practiced to occlude and prevent rupture of an aneurysm. Surgical clipping involves placing a surgical clip across the neck of an aneurysm during open surgery to prevent blood flow into the aneurysm. Endovascular treatments include standard coiling and

using a stent as a flow diverter, which are both minimally invasive procedures, using a catheter to either place coils in the aneurysm or a stent across the neck of the aneurysm [13, 23, 24, 58].

The endovascular treatment of using a stent as a flow diverter first appeared in 2006. The porous design of the stent device and placement across the neck of an aneurysm changes the hemodynamics by reducing the blood flow into the aneurysm, which induces flow stagnation and thrombosis within the aneurysm. Figure 1.1 shows the change in blood flow induced by the placement of a stent across the neck of the aneurysm. The series of pictures illustrates the aneurysm before stenting, immediately after stenting, and 6 months after stenting. Complete aneurysm occlusion does not occur rapidly, as is the case with other treatment options, but instead may take 3 to 6 months with the stent in place. Initial trials indicate 49–95% complete occlusion after 6 months using stent treatment. However, further validation of stent treatment safety and efficacy is required. Computational studies that model the hemodynamics in an artery with an aneurysm and stent contribute to the further understanding of the effectiveness of stent treatment [58, 21, 24].

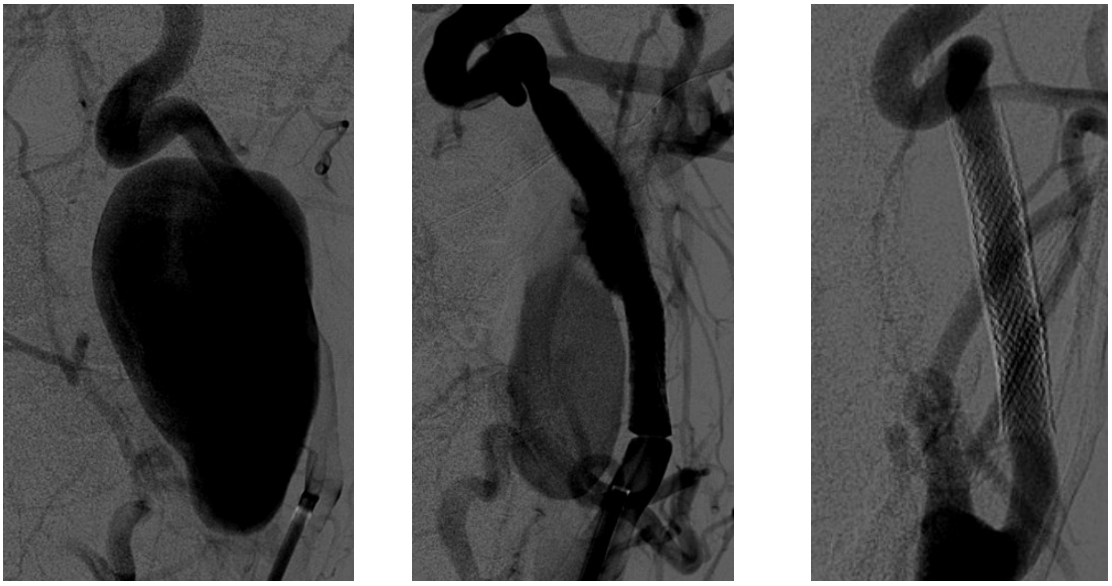

Before Stenting Immediately After Stenting 6 Months After Stenting

Figure 1.1: Sequence of 3DRA images showing aneurysm treated with stent.

The following study summarizes the special arterial fluid mechanics techniques developed for computations involving patient-specific cerebral arteries with aneurysm and stent and investigates how the unsteady flow patterns in the aneurysm are influenced by the presence of single and double stents. We compare various characteristics of blood flow into and within the aneurysm to determine the effect of the stent in promoting thrombosis. Additionally, we compare the flow patterns obtained with finite- and zero-thickness representations of the stent.

1.2 Overview

Chapter 2 provides the Navier–Stokes equations of incompressible flow, which are the governing equations for blood flow, and the Deforming-Spatial-Domain/Stabilized Space–Time (DSD/SST) formulation with variational multiscale (VMS) method, which is the finite element solution technique for the fluid mechanics.

Chapter 3 describes the special modeling and mesh generation techniques, focusing specifically on the mesh generation of the stent.

Chapter 4 explains the fluid properties and boundary and simulation conditions specified for the computations.

Chapter 5 shows the results of the study investigating the change in blood flow patterns induced by the presence of either single or double stents. The comparison between the finite- and zero-thickness representations of the stent are also shown here.

Chapter 6 offers concluding remarks.

Chapter 2

Governing Equations and Finite Element Formulation

The study of arterial fluid mechanics is inherently a FSI problem where both the blood flow and arterial wall deformation are each influenced by the other. In the following study of cerebral aneurysms treated with a stent, however, we hold the arterial wall rigid and compute the fluid mechanics independently. Section 2.1 shows the Navier–Stokes equations of incompressible flow which govern the fluid mechanics. The DSD/SST formulation with the VMS method is described in Section 2.2.

Although the focus of this study depends predominantly on fluid mechanics computations, obtaining the initial arterial geometry requires arterial wall deformation governed by the structural mechanics equations given in [33] modeled with a hyperelastic continuum element made of Fung material [43].

2.1 Fluid Mechanics

Blood flow is known to be non-Newtonian in nature, yet when considering blood flow in cerebral arteries we assume it to be Newtonian. The cerebral arterial diameters and flow rates considered yield an average shear rate greater than 150 s^{-1}. It was

explained in [50] that we can approximate viscosity as a constant if the shear rate is large enough ($> 150\ \mathrm{s}^{-1}$) [56].

Let $\Omega_t \subset I\!R^{n_{sd}}$ be the spatial domain with boundary Γ_t at time $t \in (0,T)$. The subscript t indicates the time-dependence of the domain. The Navier–Stokes equations of incompressible flows are written on Ω_t and $\forall t \in (0,T)$ as

$$\rho\left(\frac{\partial \mathbf{u}}{\partial t} + \mathbf{u}\cdot\boldsymbol{\nabla}\mathbf{u} - \mathbf{f}\right) - \boldsymbol{\nabla}\cdot\boldsymbol{\sigma} = \mathbf{0}, \tag{2.1}$$

$$\boldsymbol{\nabla}\cdot\mathbf{u} = 0, \tag{2.2}$$

where ρ, $\mathbf{u}$ and $\mathbf{f}$ are the density, velocity and the external force, respectively. The stress tensor $\boldsymbol{\sigma}$ is defined as $\boldsymbol{\sigma}(p,\mathbf{u}) = -p\mathbf{I} + 2\mu\boldsymbol{\varepsilon}(\mathbf{u})$, with $\boldsymbol{\varepsilon}(\mathbf{u}) = \left((\boldsymbol{\nabla}\mathbf{u}) + (\boldsymbol{\nabla}\mathbf{u})^T\right)/2$. Here p is the pressure, $\mathbf{I}$ is the identity tensor, $\mu = \rho\nu$ is the viscosity, ν is the kinematic viscosity, and $\boldsymbol{\varepsilon}(\mathbf{u})$ is the strain-rate tensor. The essential and natural boundary conditions for Eq. (2.1) are represented as $\mathbf{u} = \mathbf{g}$ on $(\Gamma_t)_{\mathrm{g}}$ and $\mathbf{n}\cdot\boldsymbol{\sigma} = \mathbf{h}$ on $(\Gamma_t)_{\mathrm{h}}$, where $(\Gamma_t)_{\mathrm{g}}$ and $(\Gamma_t)_{\mathrm{h}}$ are complementary subsets of the boundary Γ_t, $\mathbf{n}$ is the unit normal vector, and $\mathbf{g}$ and $\mathbf{h}$ are given functions. A divergence-free velocity field $\mathbf{u}_0(\mathbf{x})$ is specified as the initial condition.

2.2 DSD/SST-VMST (ST-VMS) Formulation of Fluid Mechanics

A space–time variational formulation of incompressible flows (see for example [34, 36, 37, 35, 39, 32]) is written over a sequence of N space–time slabs Q_n, where Q_n is the slice of the space–time domain between the time levels t_n and t_{n+1}, and P_n is the lateral boundary of Q_n. We denote the trial and test functions spaces for the velocity and pressure as $\mathbf{u} \in \mathcal{S}_{\mathbf{u}}$, $p \in \mathcal{S}_p$, $\mathbf{w} \in \mathcal{V}_{\mathbf{u}}$ and $q \in \mathcal{V}_p$. The notation $(\cdot)_n^-$ and $(\cdot)_n^+$ denotes the function values at t_n as approached from below and above. At each time

step, the integrations are performed over Q_n. The essential and natural boundary conditions are enforced over $(P_n)_{\rm g}$ and $(P_n)_{\rm h}$, the complementary subsets of the lateral boundary of the space–time slab. In the DSD/SST method [34, 36, 37, 35, 39, 32], the space–time finite element interpolation functions are continuous within a space–time slab, but discontinuous from one space–time slab to another. Each Q_n is decomposed into elements Q_n^e, where $e = 1, 2, \ldots, (n_{el})_n$. The subscript n used with n_{el} is for the general case where the number of space–time elements may change from one space–time slab to another. The finite-dimensional trial and test functions spaces are denoted as $\left(\mathcal{S}_{\mathbf{u}}^h\right)_n$, $\left(\mathcal{S}_p^h\right)_n$, $\left(\mathcal{V}_{\mathbf{u}}^h\right)_n$ and $\left(\mathcal{V}_p^h\right)_n$.

The DSD/SST-VMST method is given as

$$
\begin{aligned}
&\int_{Q_n} \mathbf{w}^h \cdot \rho \left(\frac{\partial \mathbf{u}^h}{\partial t} + \boldsymbol{\nabla} \cdot (\mathbf{u}^h \mathbf{u}^h) - \mathbf{f}^h \right) dQ + \int_{Q_n} \boldsymbol{\varepsilon}(\mathbf{w}^h) : \boldsymbol{\sigma}(p^h, \mathbf{u}^h) dQ \\
&- \int_{(P_n)_{\rm h}} \mathbf{w}^h \cdot \mathbf{h}^h dP + \int_{Q_n} q^h \boldsymbol{\nabla} \cdot \mathbf{u}^h dQ + \int_{\Omega_n} (\mathbf{w}^h)_n^+ \cdot \rho \left((\mathbf{u}^h)_n^+ - (\mathbf{u}^h)_n^- \right) d\Omega \\
&- \sum_{e=1}^{(n_{el})_n} \int_{Q_n^e} \left[\rho \left(\frac{\partial \mathbf{w}^h}{\partial t} + \mathbf{u}^h \cdot \boldsymbol{\nabla} \mathbf{w}^h \right) + \boldsymbol{\nabla} q^h \right] \cdot \mathbf{u}' dQ - \sum_{e=1}^{(n_{el})_n} \int_{Q_n^e} \boldsymbol{\nabla} \cdot \mathbf{w}^h p' dQ \\
&- \sum_{e=1}^{(n_{el})_n} \int_{Q_n^e} \rho \mathbf{u}' \cdot \left(\boldsymbol{\nabla} \mathbf{w}^h \right) \cdot \mathbf{u}^h dQ - \sum_{e=1}^{(n_{el})_n} \int_{Q_n^e} \rho \mathbf{u}' \cdot \left(\boldsymbol{\nabla} \mathbf{w}^h \right) \cdot \mathbf{u}' dQ = 0,
\end{aligned}
\tag{2.3}
$$

where

$$
\mathbf{u}' = -\frac{\tau_{\rm M}}{\rho} \mathbf{r}_{\rm M} \left(\mathbf{u}^h, p^h \right), \qquad p' = -\rho \nu_{\rm C} r_{\rm C} \left(\mathbf{u}^h \right), \tag{2.4}
$$

and

$$
\mathbf{r}_{\rm M} (\mathbf{u}, p) = \rho \left(\frac{\partial \mathbf{u}}{\partial t} + \mathbf{u} \cdot \boldsymbol{\nabla} \mathbf{u} - \mathbf{f} \right) + \boldsymbol{\nabla} p - 2 \boldsymbol{\nabla} \cdot \mu \boldsymbol{\varepsilon}(\mathbf{u}), \tag{2.5}
$$

$$
r_{\rm C} (\mathbf{u}) = \boldsymbol{\nabla} \cdot \mathbf{u}, \tag{2.6}
$$

and $\tau_{\rm M}$ and $\nu_{\rm C}$ are stabilization parameters closely related to $\tau_{\rm SUPG}/\tau_{\rm PSPG}$ and $\nu_{\rm LSIC}$.

There are various ways of defining τ_{M} and ν_{C}, including those in [1]. For τ_{M} we use the τ_{SUPG} definition given by Eqs. (7)–(11) in [39]. For ν_{C}, we use the ν_{LSIC} definition given by Eq. (37) in [29].

Remark 1 *The original DSD/SST formulation was named DSD/SST-SUPS in [32] (i.e. the version with the SUPG/PSPG stabilization).*

Remark 2 *If we exclude the last two terms, the formulation becomes the same as the modified DSD/SST-SUPS formulation (where the advection term is in the conservation-law form) under the conditions* $\tau_{PSPG} = \tau_{SUPG}$ *and* $\nu_{\mathrm{C}} = \nu_{LSIC}$*. The 6th and 7th terms are the Streamline-Upwind/Petrov-Galerkin (SUPG) and Pressure-Stabilizing/Petrov-Galerkin (PSPG) stabilizations and LSIC (least-squares on incompressibility constraint) term.*

Chapter 3

Special Modeling Techniques and Mesh Generation

A number of special modeling and mesh generation techniques have been developed in conjunction with the DSD/SST technique for patient-specific arterial fluid mechanics. The techniques include extracting the arterial-lumen geometry from 3DRA data [31] and generating a mesh for the lumen geometry, calculating an estimated zero-pressure (EZP) arterial geometry [38, 41, 28, 44, 30, 43, 27], using variable arterial wall thickness [28, 44, 30], and building layers of refined fluid mechanics mesh near the arterial walls [42, 28, 44, 30]. Further methods include a mapping technique for specifying the velocity profile at an inflow boundary with non-circular shape [28, 44], a new scaling technique for specifying a more realistic volumetric flow rate [43, 27], and techniques for the projection of the fluid–structure interface stresses and calculations of the wall shear stress (WSS) and oscillatory shear index (OSI) [30].

In modeling cerebral arteries with aneurysm and stent, additional modeling and mesh generation techniques were developed to address the placement of the stent across the neck of the aneurysm. Section 3.1 details the mesh generation process and describes the special techniques developed to include using NURBS for the spatial

representation of the surface over which the stent mesh is built, mesh generation techniques for both the finite- and zero-thickness representations of the stent, techniques for generating refined layers of mesh near the arterial and stent surfaces, and models for representing a double stent.

3.1 Mesh Generation

Mesh generation of the cerebral artery with aneurysm and stent requires numerous steps taking the flat-stent design and lumen geometry and generating a fluid volume mesh representative of a stented artery with aneurysm. We begin by mapping the flat-stent design to the deformed stent, which fits across the neck of the aneurysm. The artery is separated into two segments, parent and aneurysm. Layers of refined mesh are generated at the stent and arterial walls in both segments. After the remaining volume in each segment is generated, the two segments are merged on the interior-boundary mesh containing the stent.

1. Prepare lumen geometry and flat-stent model as shown in Figure 3.1. We extract the arterial surface geometry from medical images and generate a lumen geometry reflective of the inflated arterial-wall structure through the process reported in [31]. The flat-stent model was generated using the geometry of a Cordis Precise Pro Rx nitinol self-expanding stent (PC0630RXC) with a wire diameter of approximately 0.1 mm.

2. Generate a NURBS surface slightly larger than the artery such that the surface intersects the lumen geometry as shown in Figure 3.2. We swept a NURBS surface following the curvature of the parent artery and extending slightly beyond the aneurysm neck. To simplify the mesh generation process, we only model the portion of the stent crossing the neck of the aneurysm. The intersection of the

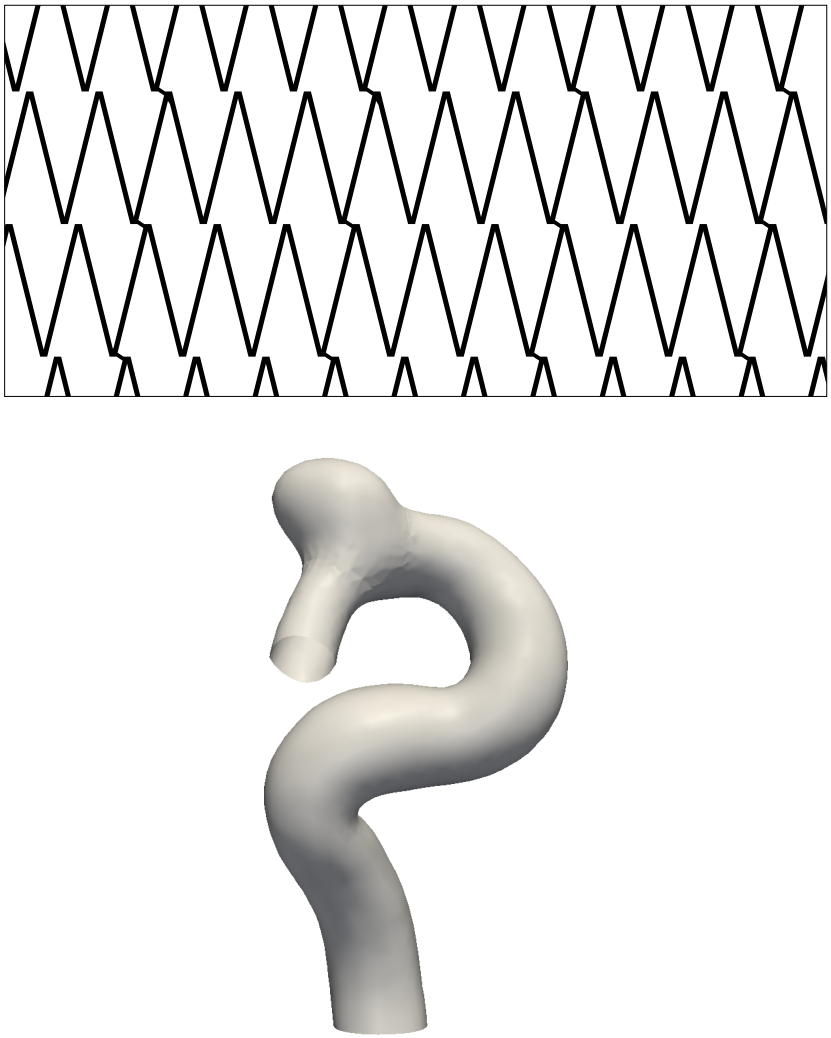

Figure 3.1: Flat-stent geometry (top) and arterial lumen geometry (bottom).

NURBS surface and lumen geometry is the periphery of the interior boundary containing the stent.

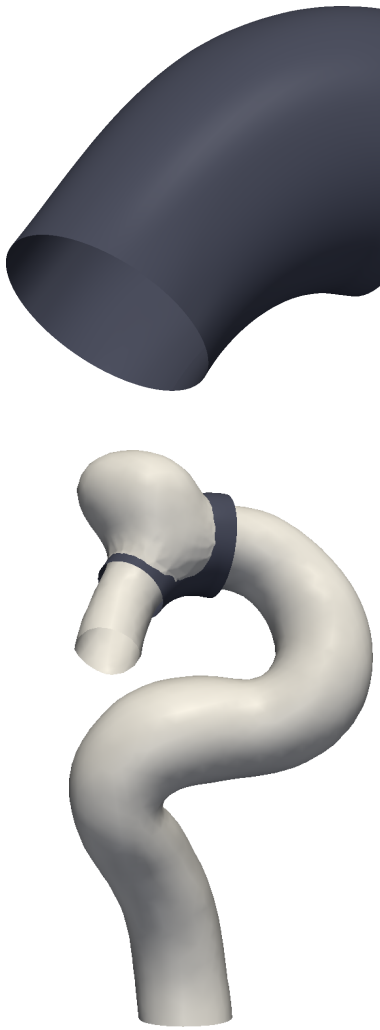

Figure 3.2: Deformed stent (top) and split lumen geometry with the stent (bottom).

3. Map the periphery of the interior boundary, described above, to the flat stent and mesh that as shown in Figure 3.3. We generate a triangular surface mesh using ANSYS and the geometry defined by the flat stent and interior-boundary periphery. The maximum element size specified in ANSYS mesh generation leads to the width of the stent wire being meshed with 3 to 4 elements. This ensures sufficient refinement to resolve the flow on the stent. The flat-stent

mesh is then mapped from the flat NURBS surface to the deformed NURBS surface to form the interior-boundary mesh positioned across the neck of the aneurysm.

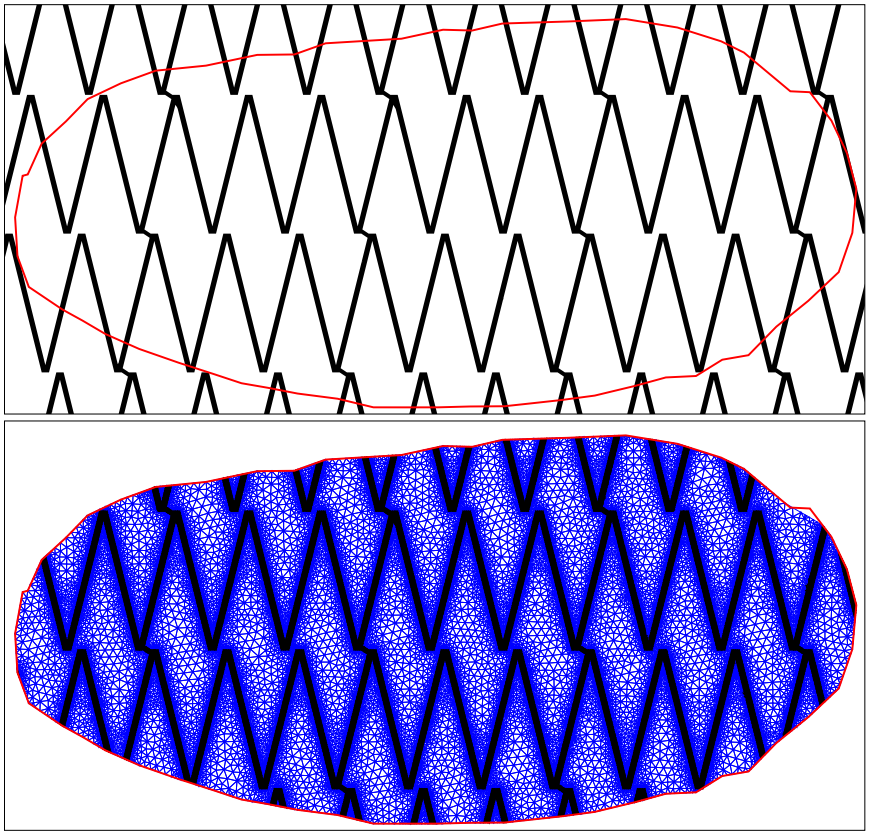

Figure 3.3: Flat stent with the periphery of the interior-boundary geometry (top) and stent mesh (bottom).

4. Use the periphery of the interior-boundary mesh as a predefined set of element edges, splitting the lumen geometry into parent and aneurysm segments as shown in Figure 3.4. This reduces complexity in mesh generation. We use ANSYS to generate the triangular surface meshes on the parent and aneurysm segments.

5. Using the surface meshes for the parent and aneurysm segments, we generate layers of refined mesh on either side of the stent and near the arterial walls. We use the process reported in [31] to generate the layers in the parent segment.

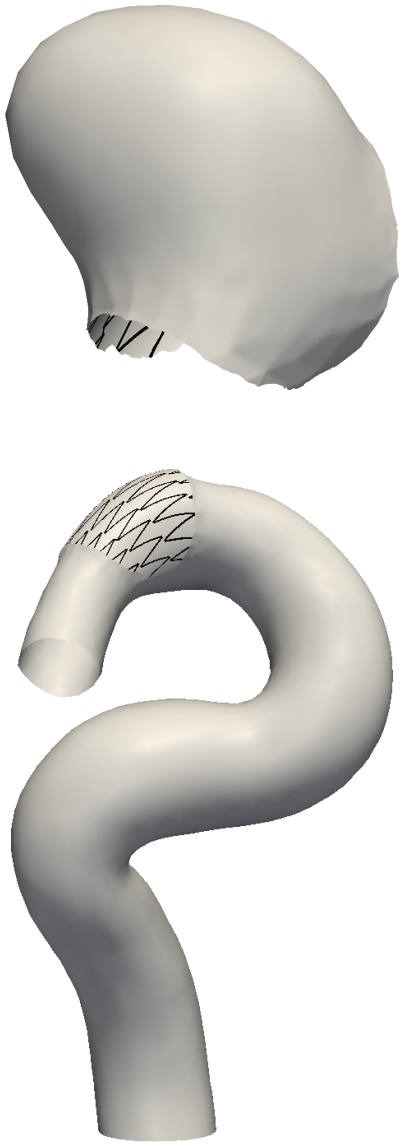

Figure 3.4: Aneurysm artery segment (top) and parent artery segment (bottom), separated by the stent.

In generating the layers in the aneurysm segment, we first start by separating the surface mesh into different regions as shown in Figure 3.5. Due to the sharp angle of the geometry, no layers are explicitly generated in the red region. We specify a uniform thickness for the layers of refined mesh in the blue regions. The thickness of the first layer is approximately equal to the first layer of refined mesh in the parent segment. There are a total of 4 layers, each increasing in thickness using a progression ratio of 1.75 (the same number of layers and progression ratio used in [31]). To prevent elements tangling, the Laplace's equation is solved over the green region of the surface mesh to determine the thickness growth from essentially zero at the boundary with the red region to the desired layer thickness at the blue region boundary. We generate each of the 4 layers in the aneurysm segment separately and merge the layers (see Remark 4).

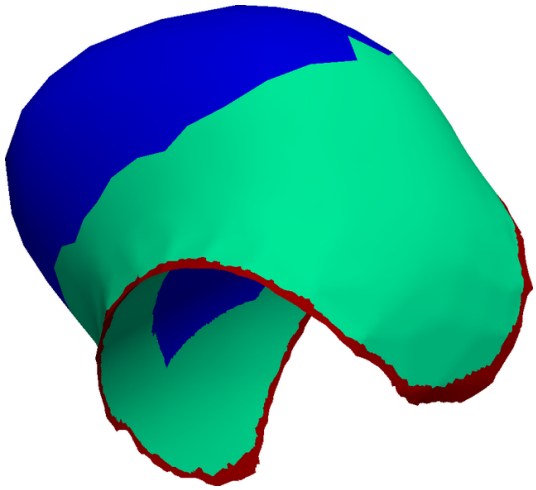

Figure 3.5: Aneurysm artery segment showing regions of different thickness for the layers of refined mesh.

6. The rest of the fluid mechanics volume mesh is generated using ANSYS. The innermost surface of the layers of refined mesh is extracted from the volume mesh and used as the surface mesh for generating the volume mesh in both the

parent and aneurysm segments. The inner volume mesh is then merged to the refined layers.

7. The parent and aneurysm fluid volume mesh segments are merged on the interior-boundary mesh containing the stent. For the no-stent cases, all nodes are merged on that interior-boundary mesh. For the single- and double-stent cases, the nodes on the stent portion of the interior-boundary mesh are not merged and instead colocated.

Remark 3 *We generate the double stent by overlaying two single flat-stent geometries and translating one of the geometries in two directions. We map the intersection of the deformed NURBS surface and lumen geometry, which is again the periphery of the interior boundary, to the flat double-stent geometry and mesh the double stent as one mesh. The double-stent mesh is treated the same as the single-stent mesh in the remaining mesh generation steps. Figure 3.6 shows the full single and double stents, respectively.*

Remark 4 *The mesh generation process for the layers of refined mesh in the aneurysm segment presents challenges regarding tangled elements. With the mesh refinement required by the problem, building the layers into the artery has the potential to create elements with negative Jacobians. Each layer must be checked for the Jacobian values before generating the next layer.*

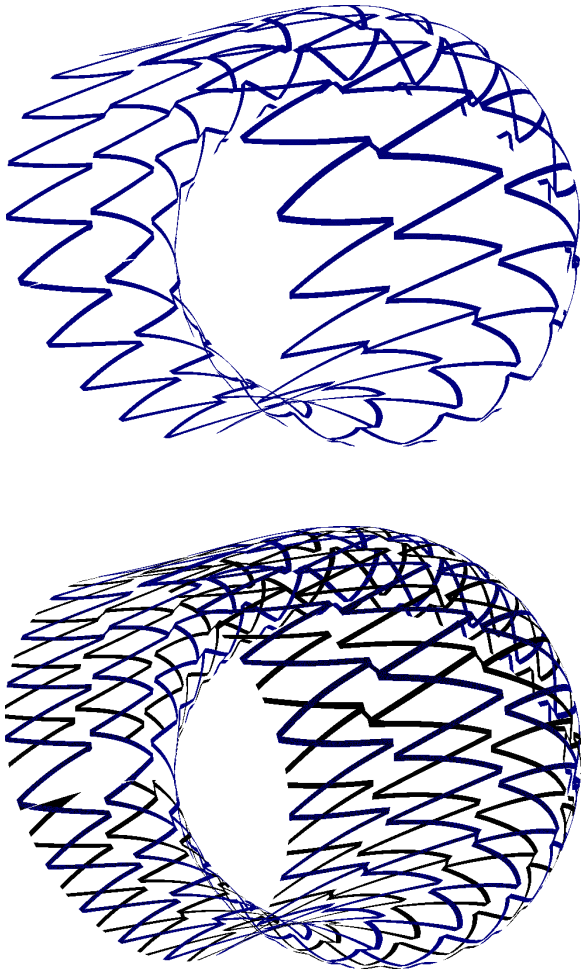

Figure 3.6: Surface for single stent (top) and double stent (bottom).

Chapter 4

Simulation Conditions

The fluid properties and boundary and computational conditions for the stent cases are given in Sections 4.1–4.3. The structural properties and outflow conditions used in the initial artery inflation are reported in [43].

4.1 Fluid Properties

Blood is assumed to behave like a Newtonian fluid as described in Section 2.1 and previously reported in [46, 47, 48, 49, 50]. The blood viscosity and kinematic viscosity are set to 1,000 kg/m^3 and 4.0×10^{-6} m^2/s, respectively.

4.2 Boundary Conditions

As was pointed out in and reproduced from [43], we specify the velocity profile as a function of time at the inflow boundary, by using the technique introduced in [28]. For completeness, we describe the technique from [28]. We use a velocity waveform which represents the cross-sectional maximum velocity as a function of time. Assuming that the maximum velocity occurs at $r = 0$, the artery is rigid and the cross-sectional

shape is a perfect circle, we can apply the Womersley [57] solution as follows:

$$U^{\mathrm{P}}(r,t) = A_0\left(1-\left(\frac{r}{r_{\mathrm{B}}}\right)^2\right) + \sum_{k=1}^{N} A_k \frac{J_0(\alpha\sqrt{k}\imath^{\frac{3}{2}}) - J_0(\alpha\sqrt{k}\left(\frac{r}{r_{\mathrm{B}}}\right)\imath^{\frac{3}{2}})}{J_0(\alpha\sqrt{k}\imath^{\frac{3}{2}}) - 1}\exp\left(\imath 2\pi k\frac{t}{T}\right), \tag{4.1}$$

where N is the number of Fourier coefficients (we use $N = 20$), $A_k \in \mathbb{C}$ are the Fourier coefficients of the waveform, T is the period of the cardiac cycle, J_0 is the Bessel functions of the first kind of order 0, $\imath$ is the imaginary number, and α is the Womersley parameter:

$$\alpha = r_{\mathrm{B}}\sqrt{\frac{2\pi}{\nu T}}. \tag{4.2}$$

We use the special mapping technique described in [28, 44] for non-circular shapes.

Remark 5 *In the current T★AFSM computations, the volumetric flow rate (which was calculated based on a velocity waveform that represents the cross-sectional maximum velocity) is scaled by a factor. The scaling factor is determined in such a way that the scaled flow rate, when averaged over the cardiac cycle, yields a target WSS for Poiseuille flow over an equivalent cross-sectional area. The target WSS is 10 dyn/cm^2 in the current T★AFSM computations.*

At all arterial outflows, we specify a stress free boundary condition. We specify no-slip boundary conditions for the flow on the arterial wall and stent.

4.3 Computational Conditions

The computations are carried out using the DSD/SST-VMST technique (see Section 2.2). The time step size is 3.333×10^{-3} s. The number of nonlinear iterations per time step is 4 and the number of GMRES iterations per nonlinear iteration is chosen such that mass balance is satisfied with essentially zero difference between inflow and outflow rates.

Chapter 5

Computational Results

Endovascular stent placement across the neck of an intracranial aneurysm can cause hemodynamic changes leading to aneurysm occlusion and thrombosis. We compare the flow field of arterial geometries before and after virtual "stenting" to assess the changes. Select aneurysms require treatment using two or more stents to sufficiently alter the flow field allowing for thrombosis. The test computations for each geometry include a before-stenting case and after-stenting cases for both single- and double-stent treatments to compare the effectiveness of stenting with multiple stents. Section 5.1 details the parameters for the four arterial geometries used in the computations. In Section 5.2 we compare hemodynamic values before and after stenting. In Section 5.3, we compare the results from modeling the stent with zero- and finite-thickness representations.

5.1 Computational Models

Four patient-specific cerebral arteries with aneurysms are studied at three states: before stenting, after stenting with a single stent deployed, and after stenting with two stents deployed. The physical parameters for the four arterial models are listed in Table 5.1 and the lumen geometries are shown in Figure 5.1.

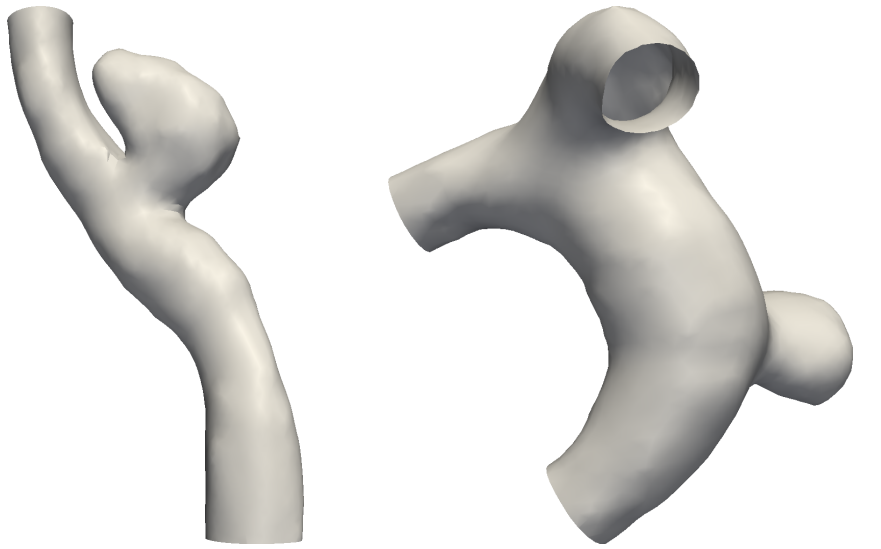

Model 1

Model 2

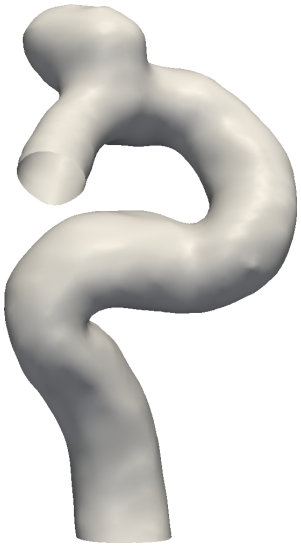

Model 3

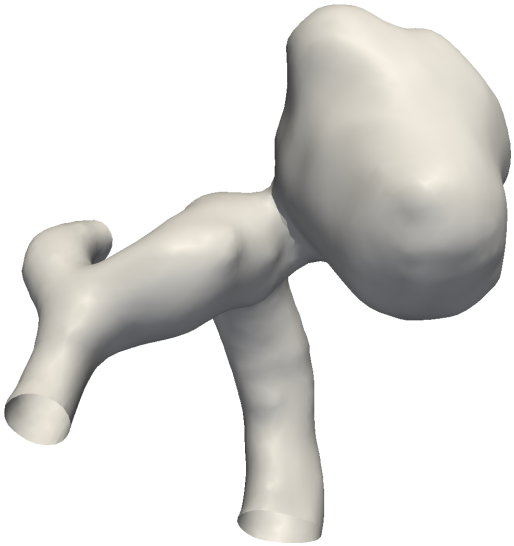

Model 4

Figure 5.1: Arterial lumen geometry obtained from voxel data for the four models studied.

Model	D_{I}	D_{O1}	D_{O2}	α	$Q_{\max}$
Model 1	0.37	0.29		2.33	2.05
Model 2	0.28	0.24	0.27	1.75	0.78
Model 3	0.44	0.26		2.73	3.40
Model 4	0.35	0.17	0.21	2.21	1.63

Table 5.1: Physical parameters for the four arterial geometries. Diameters are in cm and peak volumetric flow rate is in ml/s. Here D_{I}, D_{O1}, and D_{O2} are the diameters at the inflow, first outflow, and second outflow, respectively. Also, α and $Q_{\max}$ are Womersley number and peak volumetric flow rate, respectively.

In the computations, we use the lumen geometries obtained after the artery goes through the EZP process [43, 27] and is inflated to a pressure corresponding to the pressure at the start of our computation cycle (cardiac cycle), which is approximately 80 mm Hg in all cases computed. The fluid mechanics meshes of the single-stent case for each model are shown in Figures 5.2 and 5.3. The cross-section view shows the refined mesh at the aneurysm neck on either side of the boundary separating the aneurysm from the parent artery. The node and element numbers for the 12 fluid mechanics meshes are given in Table 5.2. We note that all computations presented in Section 5.2 are for zero-thickness representation of the stent.

The number of GMRES iterations per nonlinear iteration for each model are shown in Table 5.3. We check the mass balance as one of the indicators of numerical convergence. Sufficient mass balance is reached when the difference between the inflow and outflow rates essentially equals zero as explained in Section 4.3. Figures 5.4–5.15 show the mass balance for all cases.

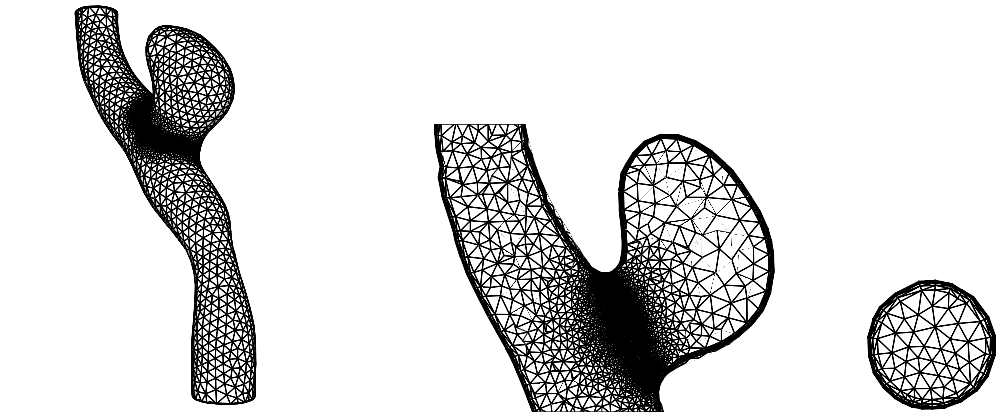

Model 1

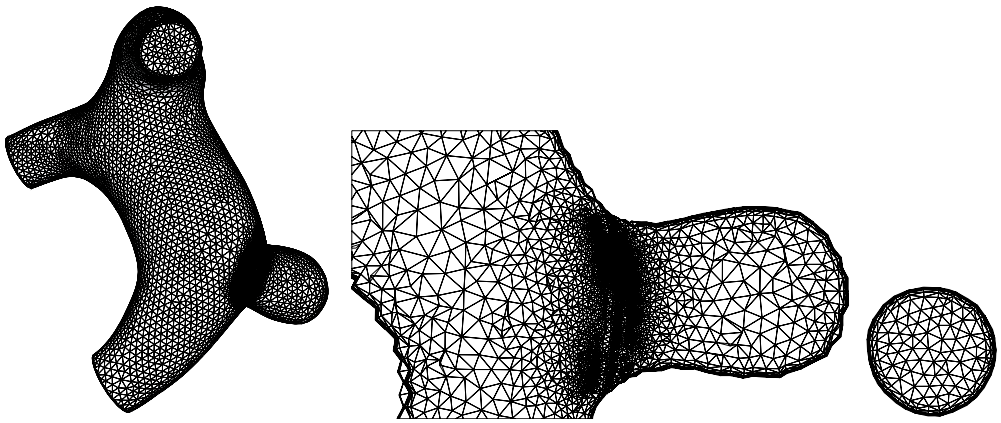

Model 2

Figure 5.2: Fluid mechanics meshes for the single-stent case for Model 1 and Model 2 with cross-section and inflow plane views.

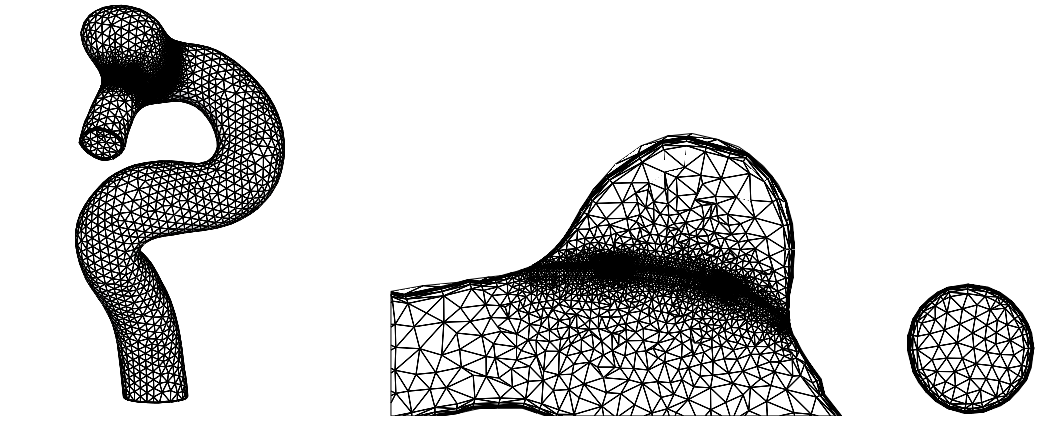

Model 3

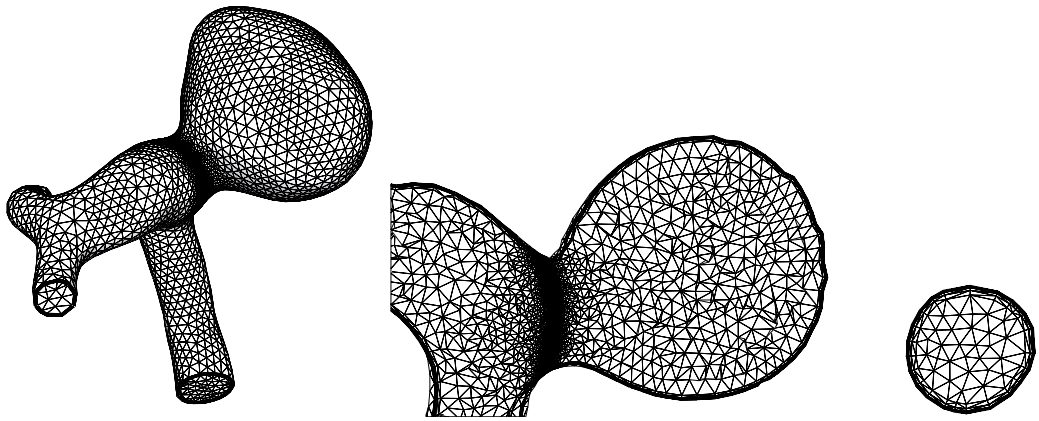

Model 4

Figure 5.3: Fluid mechanics meshes for the single-stent case for Model 3 and Model 4 with cross-section and inflow plane views.

	Model 1		Model 2	
	nn	ne	nn	ne
No Stent	527,323	3,168,305	430,497	2,532,798
Single Stent	566,049	3,300,182	442,454	2,532,798
Double Stent	662,431	3,736,603	503,819	2,823,729
	Model 3		Model 4	
	nn	ne	nn	ne
No Stent	530,268	3,136,903	428,260	2,522,129
Single Stent	552,922	3,136,903	447,430	2,522,129
Double Stent	930,403	5,261,467	867,500	4,916,931

Table 5.2: Number of nodes and elements for the fluid mechanics mesh for each case of the four arterial models. Here nn and ne are number of nodes and elements, respectively.

	Model 1	Model 2	Model 3	Model 4
No Stent	1000	1000	1500	1000
Single Stent	1500	1000	1500	1000
Double Stent	1500	1200	2000	1700

Table 5.3: GMRES iterations per nonlinear iteration for each case of the four arterial models.

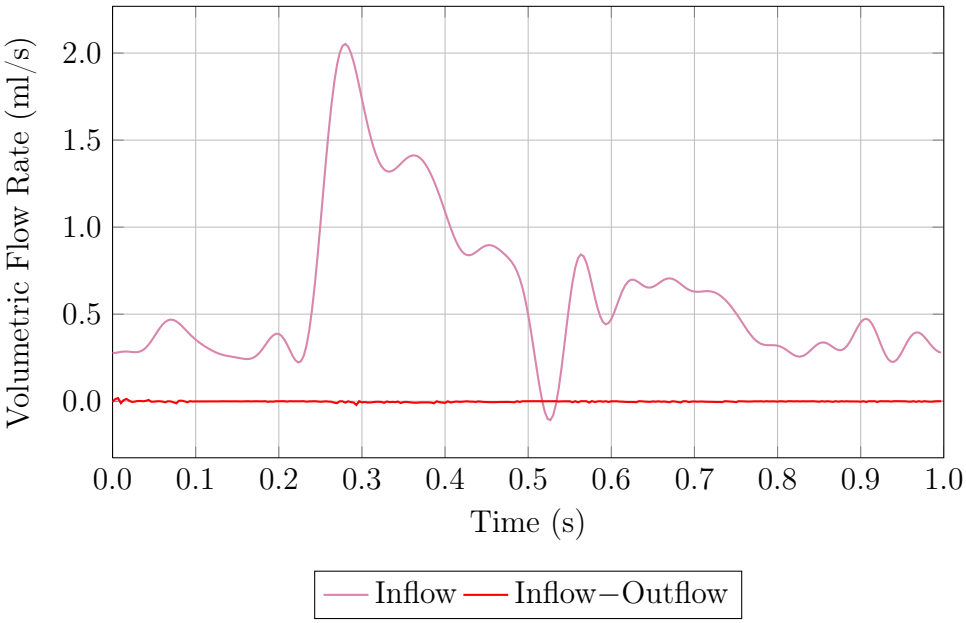

Figure 5.4: Mass balance for Model 1 before stenting.

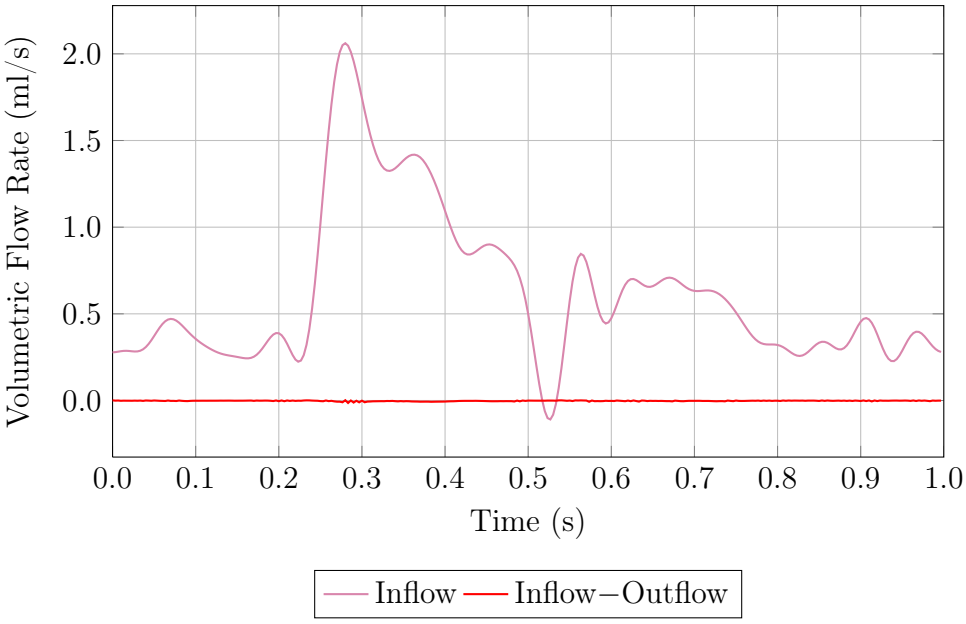

Figure 5.5: Mass balance for Model 1 with single stent deployed.

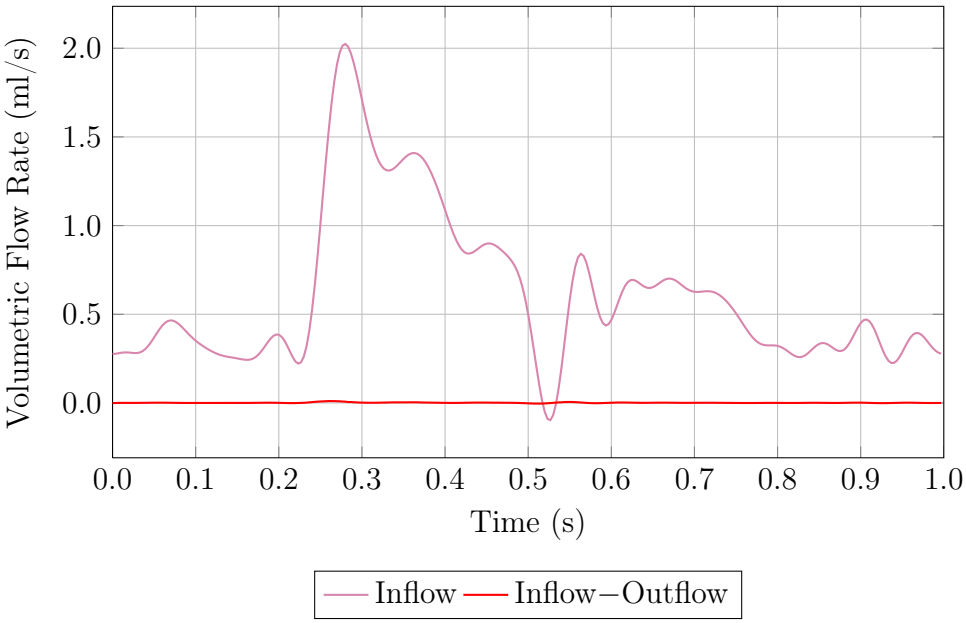

Figure 5.6: Mass balance for Model 1 with double stent deployed.

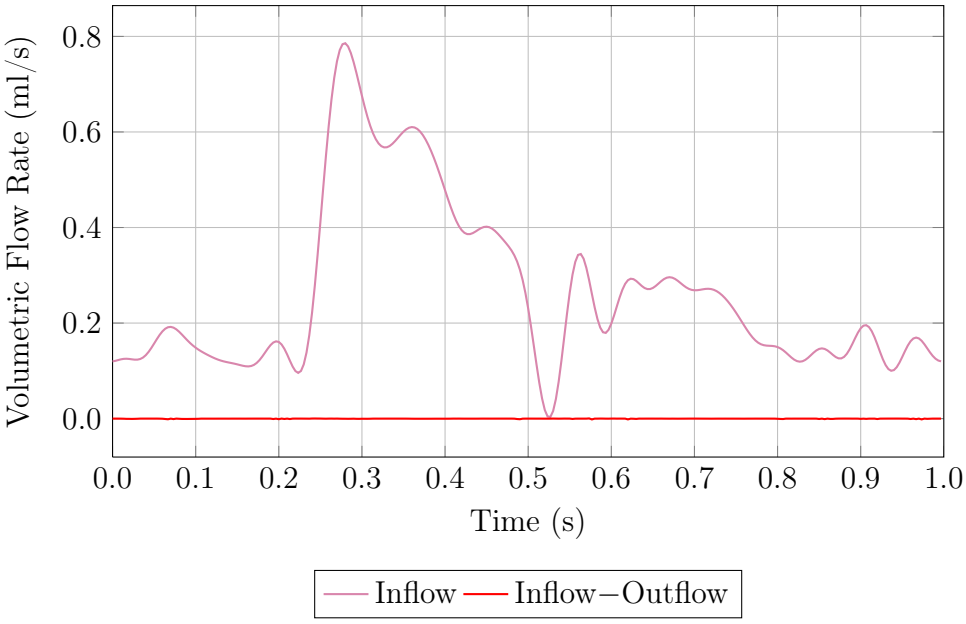

Figure 5.7: Mass balance for Model 2 before stenting.

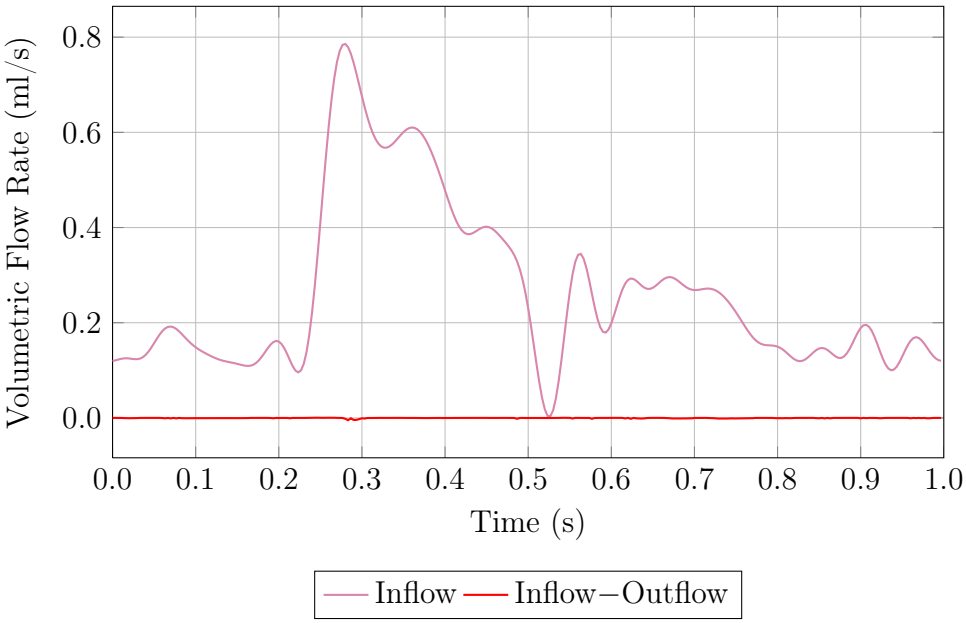

Figure 5.8: Mass balance for Model 2 with single stent deployed.

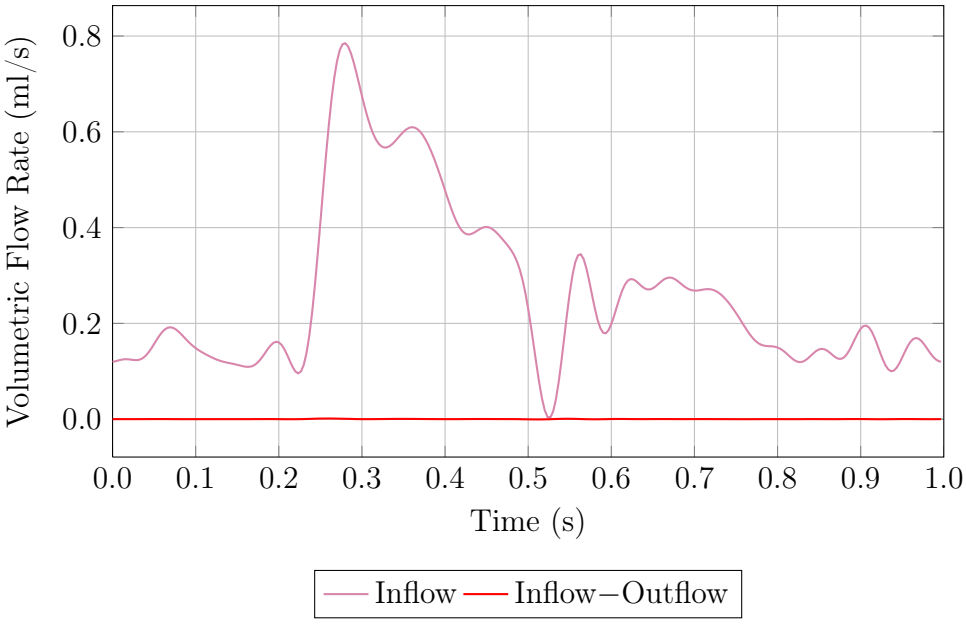

Figure 5.9: Mass balance for Model 2 with double stent deployed.

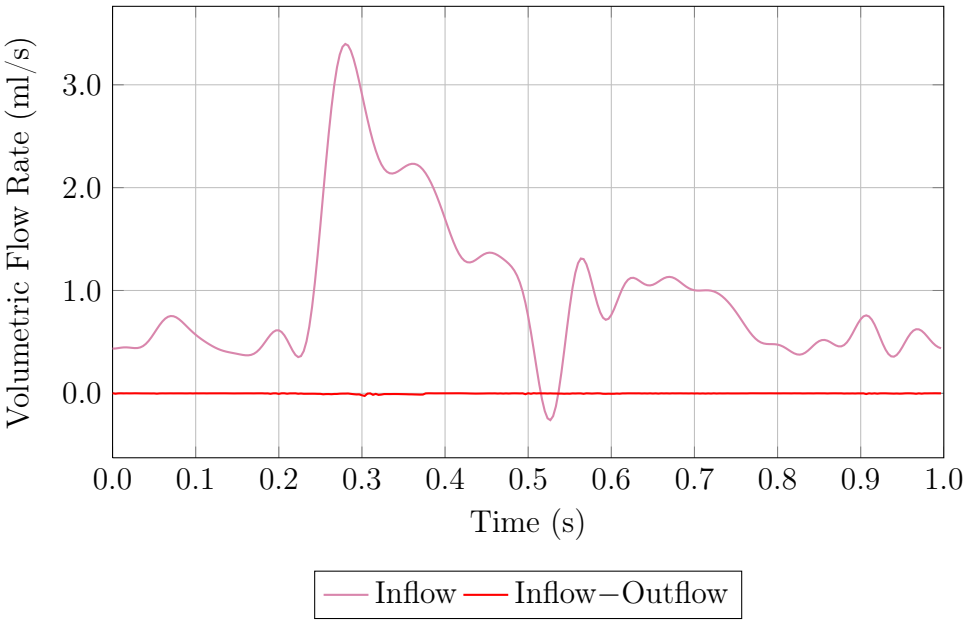

Figure 5.10: Mass balance for Model 3 before stenting.

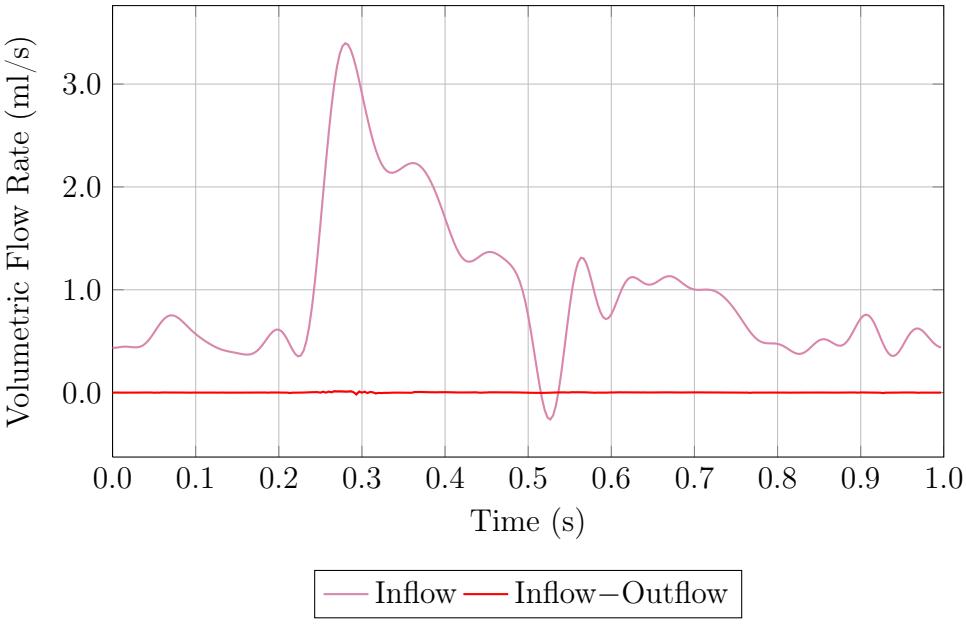

Figure 5.11: Mass balance for Model 3 with single stent deployed.

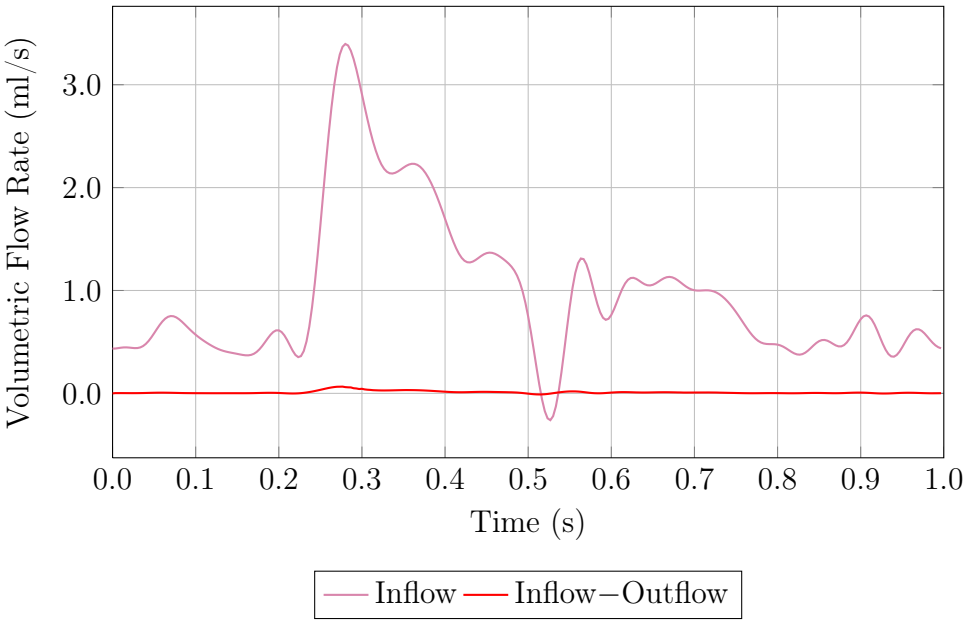

Figure 5.12: Mass balance for Model 3 with double stent deployed.

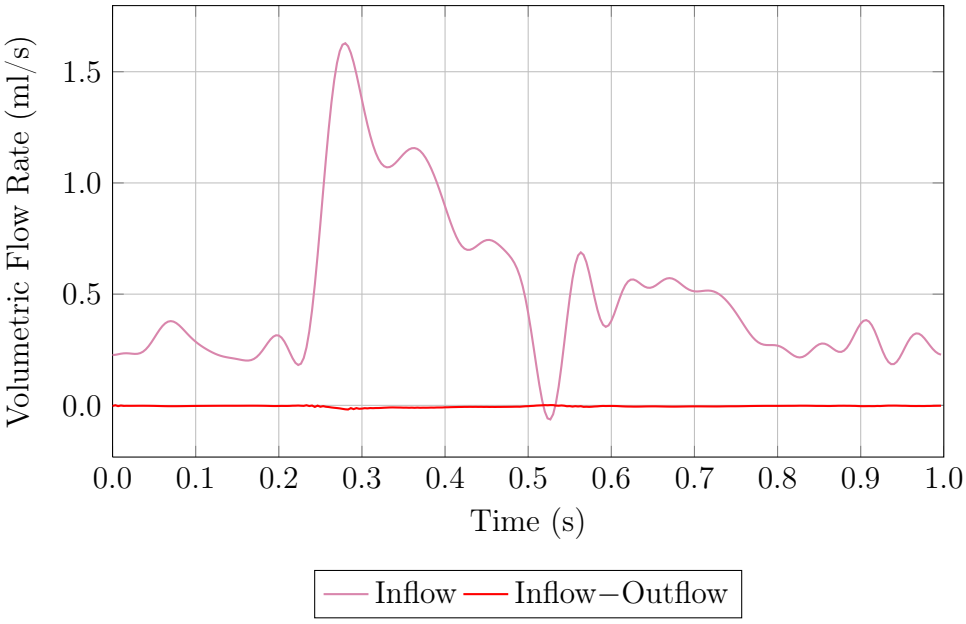

Figure 5.13: Mass balance for Model 4 before stenting.

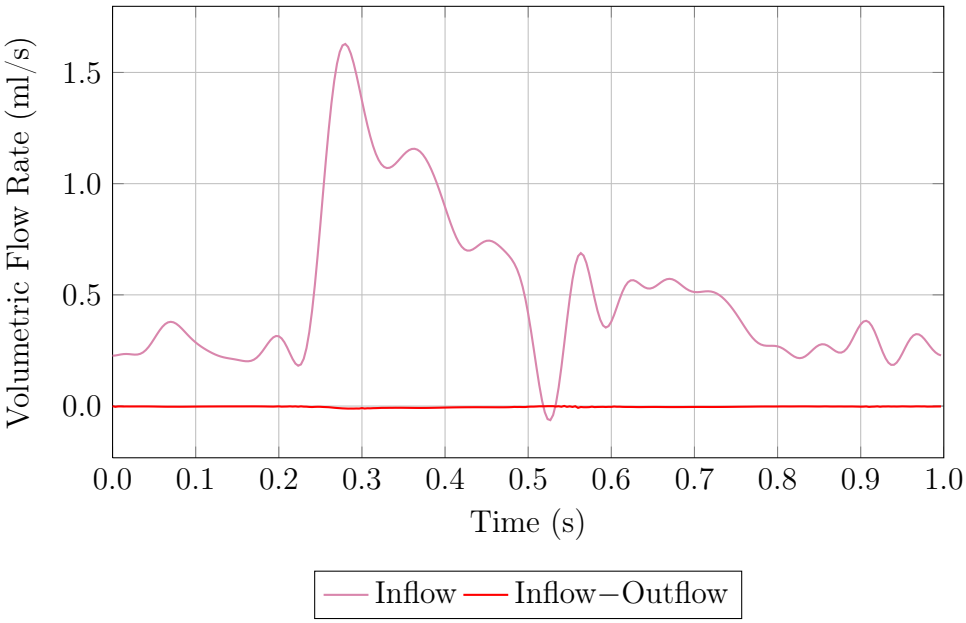

Figure 5.14: Mass balance for Model 4 with single stent deployed.

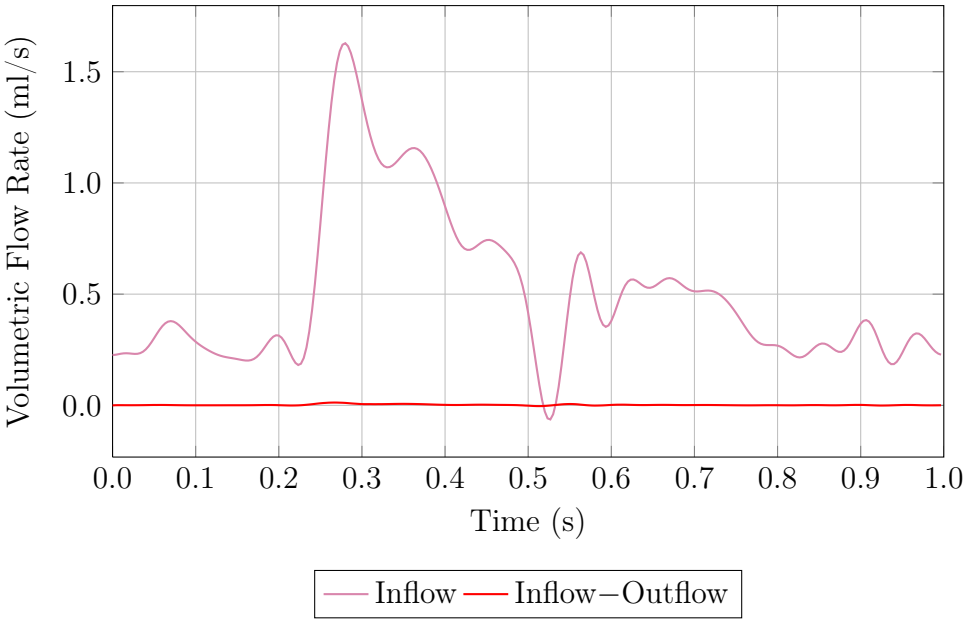

Figure 5.15: Mass balance for Model 4 with double stent deployed.

5.2 Comparative Study

Inducing thrombosis in an aneurysm requires altering the hemodynamics at the aneurysm. Inserting a stent changes the pattern and amount of blood flow from the parent artery to the aneurysm, influencing stasis within the aneurysm. The stent free area at the neck of the aneurysm is reduced to approximately 85% and 71% in the single- and double-stent cases for all four models, respectively. In the following sections, we compare the fluid mechanics before and after stenting in each of the four models by analyzing the ratio of the aneurysm-inflow rate to the time-averaged parent-artery-inflow rate $\frac{Q_A}{Q_P}$, the spatially averaged kinetic energy and vorticity in the aneurysm, and OSI. The aneurysm-inflow rate is calculated by integrating the magnitude of the normal component of the velocity over the interior-boundary mesh containing the stent and dividing that by 2. The effectiveness of stenting using either the single or double stent depends on the degree to which the flow characteristics were altered and also the arterial geometry and size of the aneurysm. The higher OSI observed in stent cases for all models follows the belief that regions with increased OSI prompt thrombus formation [22, 16].

5.2.1 Model 1

The aneurysm in Model 1 has a volume of 0.10 cm^3 and approximate neck area of 0.47 cm^2. The total area in the neck blocked by the stent in the single- and double-stent cases is 0.07 cm^2 and 0.13 cm^2, respectively. Figures 5.16–5.19 show the reduction in blood flow into and within the aneurysm caused by stenting. The parent artery has an average inflow rate of 0.62 ml/s. The peak blood flow into and within the aneurysm occurs approximately 0.02 s before peak inflow rate in the parent artery. The time-averaged $\frac{Q_A}{Q_P}$ decreases by 22% and 78% in the single- and double-stent cases, respectively. Similarly, the kinetic energy averaged in space and

time decreases by 72% in the single-stent case and 92% in the double-stent case. The reduction in vorticity in the aneurysm caused by stenting is shown in Figures 5.20 and 5.21. The vorticity, averaged in space and time, is reduced by 47% and 72% in the single- and double-stent cases, respectively. Figure 5.22 shows the OSI for all three cases.

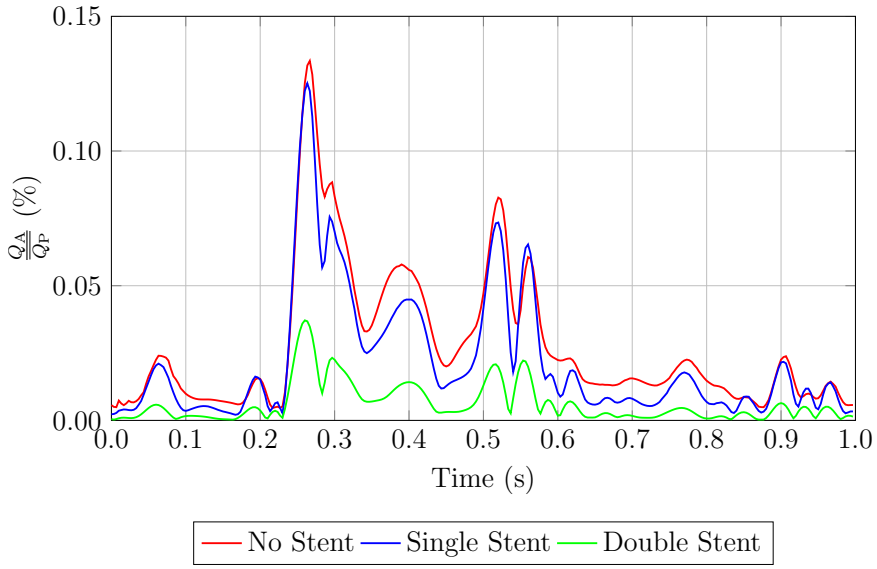

Figure 5.16: Comparison of $\frac{Q_A}{Q_P}$ for the three cases.

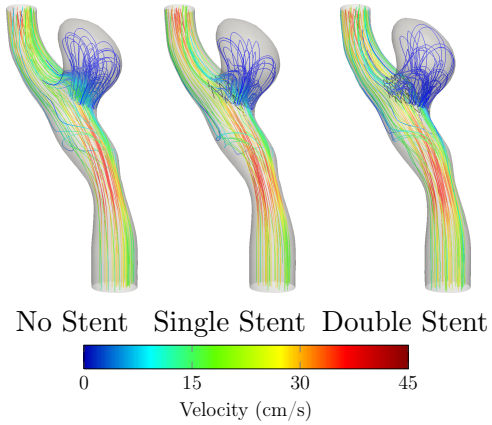

Figure 5.17: Streamlines showing changes in blood flow patterns and velocity induced by stenting at peak flow into the parent artery.

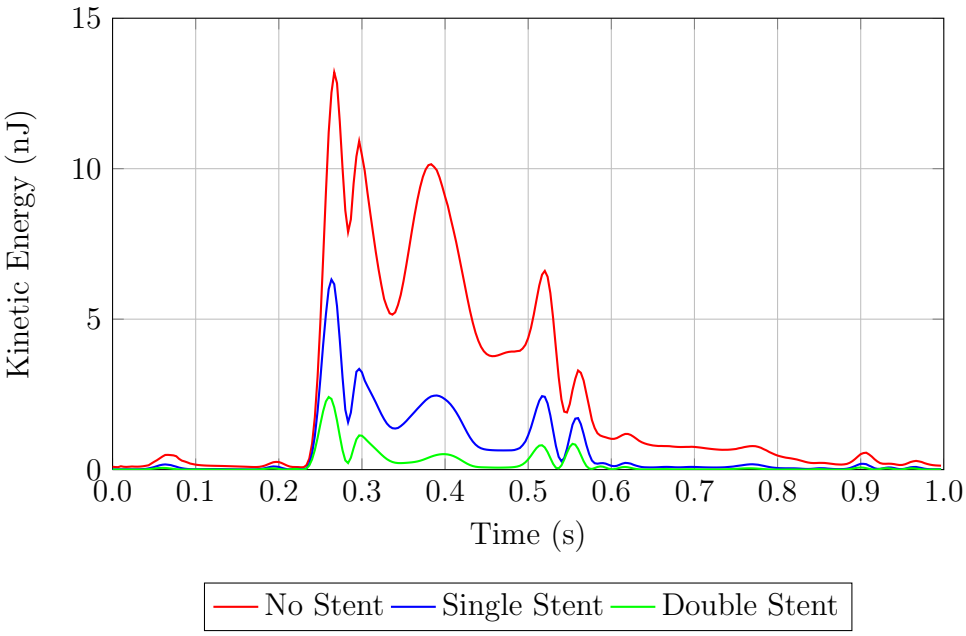

Figure 5.18: Comparison of spatially averaged kinetic energy in the aneurysm.

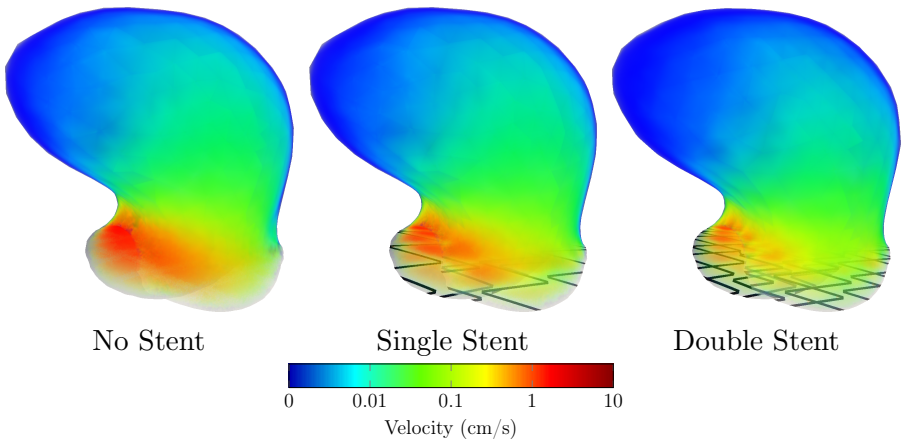

Figure 5.19: Volume rendering of aneurysm velocity magnitude at peak flow into the aneurysm.

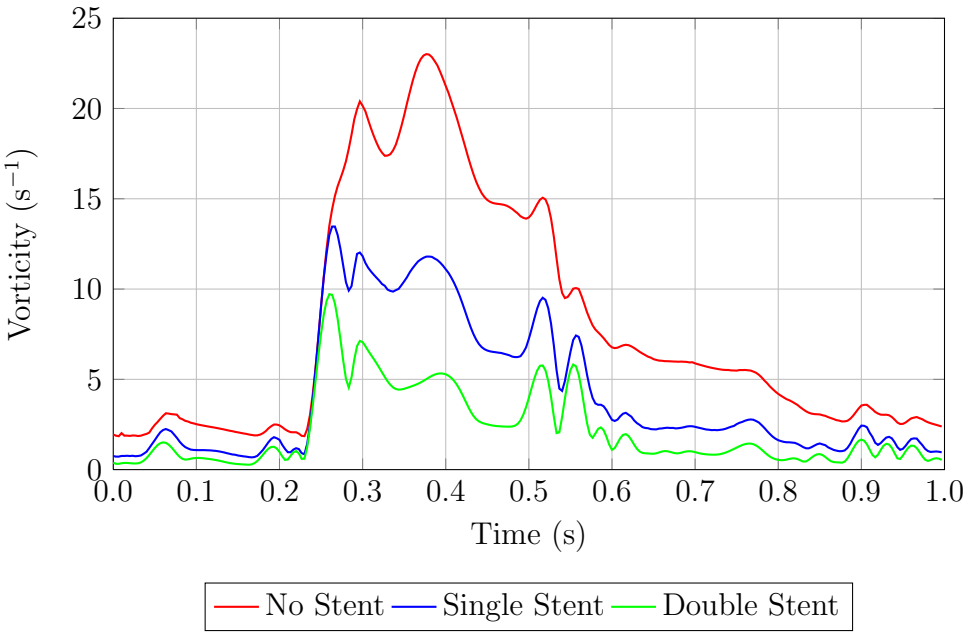

Figure 5.20: Comparison of spatially averaged vorticity magnitude in the aneurysm.

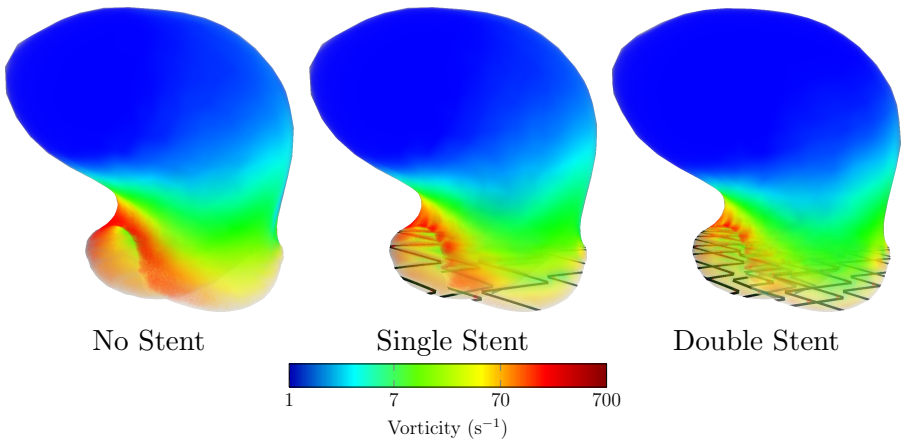

Figure 5.21: Volume rendering of aneurysm vorticity magnitude at peak flow into the aneurysm.

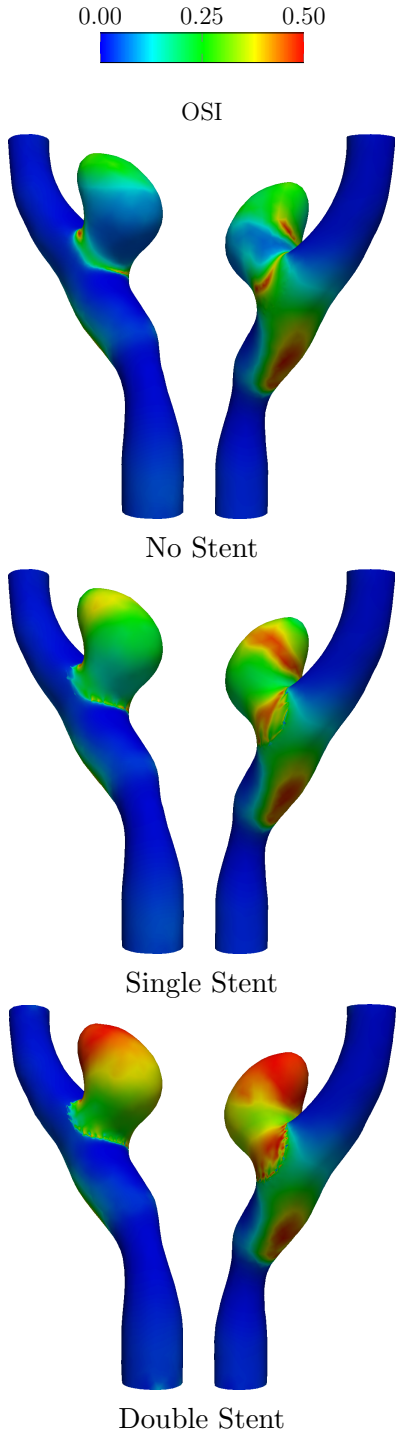

Figure 5.22: OSI for Model 1.

5.2.2 Model 2

The aneurysm in Model 2 is the smallest of the four models, computed with a volume of 0.04 cm^3 and approximate neck area of 0.36 cm^2. The stent area for the single- and double-stent cases are 0.05 cm^2 and 0.10 cm^2, respectively. The average inflow rate for Model 2 is significantly lower than the other three models at 0.26 ml/s. The change in blood flow velocity is shown in Figures 5.23–5.26. Peak blood flow into the aneurysm, along with peak kinetic energy, occurs approximately 0.13 s after peak inflow rate into the parent artery. In Figure 5.23, the time-averaged flow-rate ratio is reduced by 41% in the single-stent case and 81% in the double-stent case. As can be seen in Figure 5.25, the kinetic energy within the stent is significantly reduced with the single stent alone. The kinetic energy within the aneurysm averaged in space and time decreases by 83% and 95% in the single- and double-stent cases, respectively. The change in vorticity between the three cases is shown in Figures 5.27 and 5.28. The single-stent case exhibits a 50% reduction in vorticity averaged in space and time while the double-stent case shows a 69% reduction. Figure 5.29 shows the increase in OSI from before stenting to stenting with two stents.

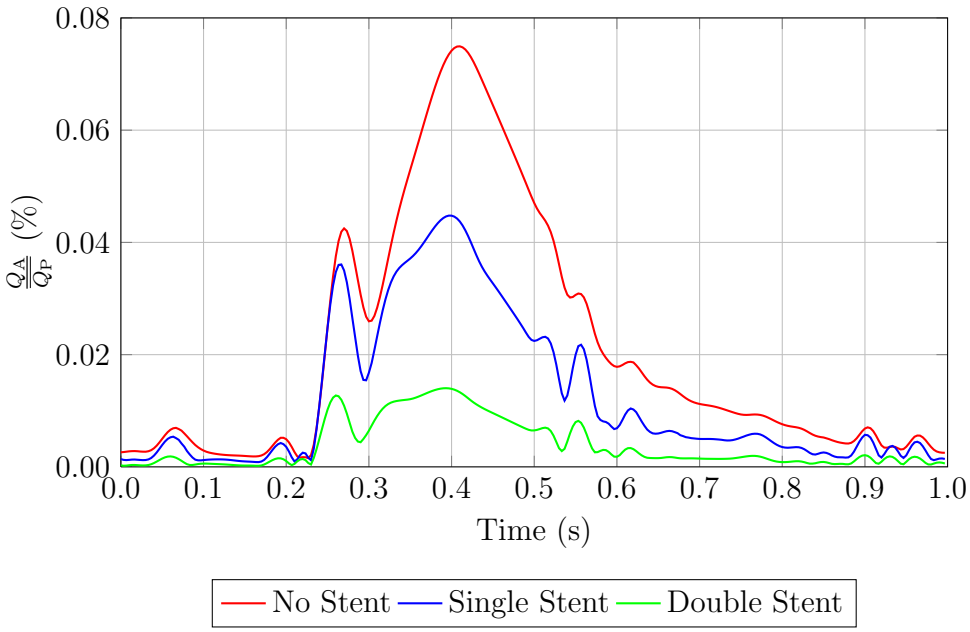

Figure 5.23: Comparison of $\frac{Q_A}{Q_P}$ for the three cases.

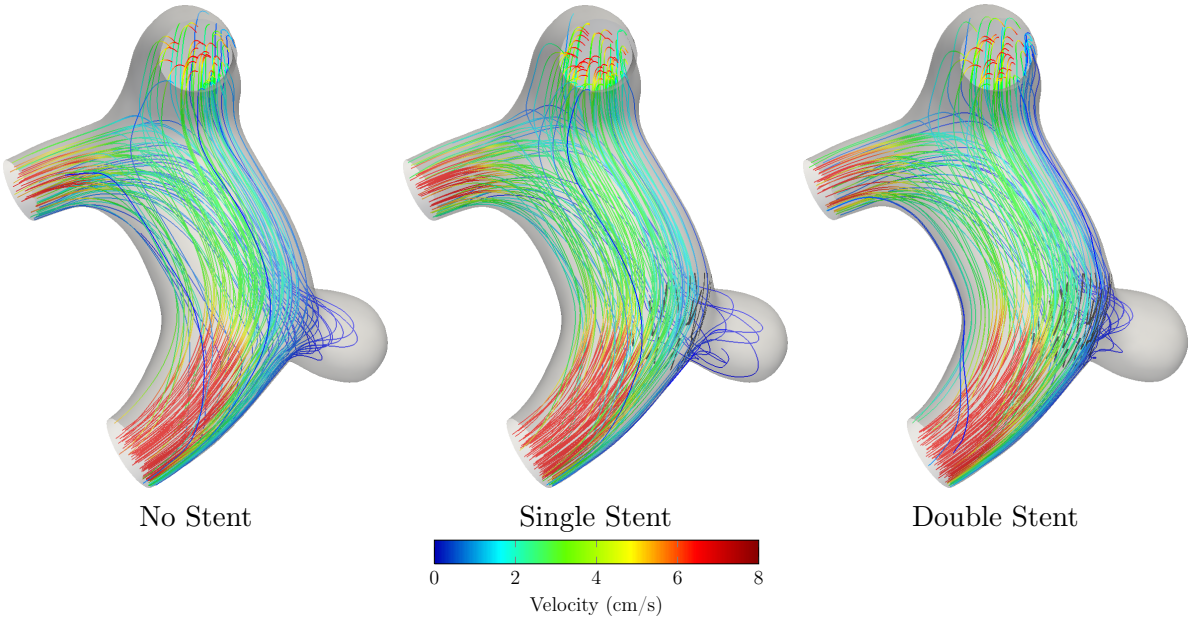

Figure 5.24: Streamlines showing changes in blood flow patterns and velocity induced by stenting at peak flow in the parent artery.

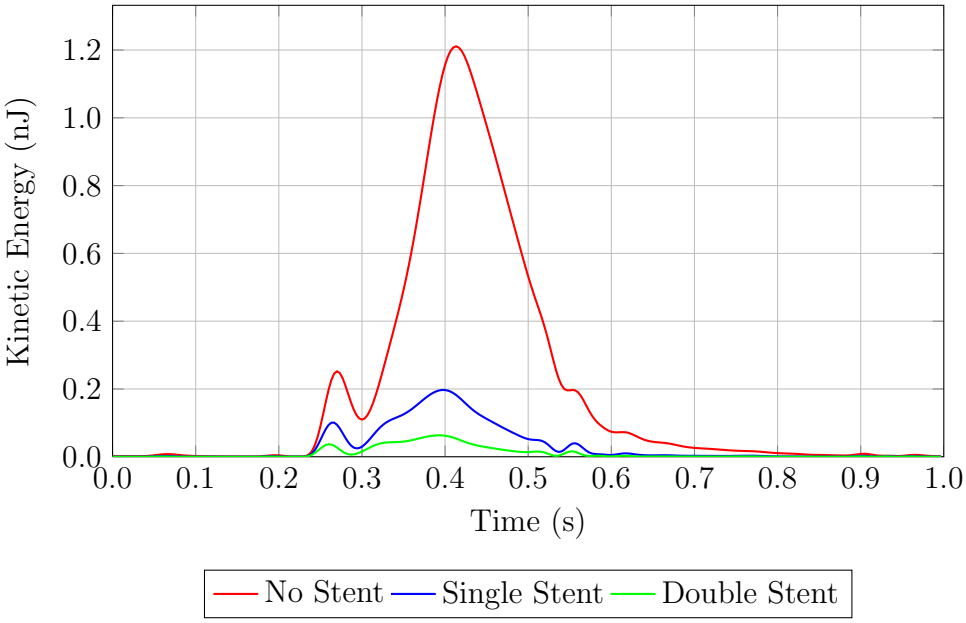

Figure 5.25: Comparison of spatially averaged kinetic energy in the aneurysm.

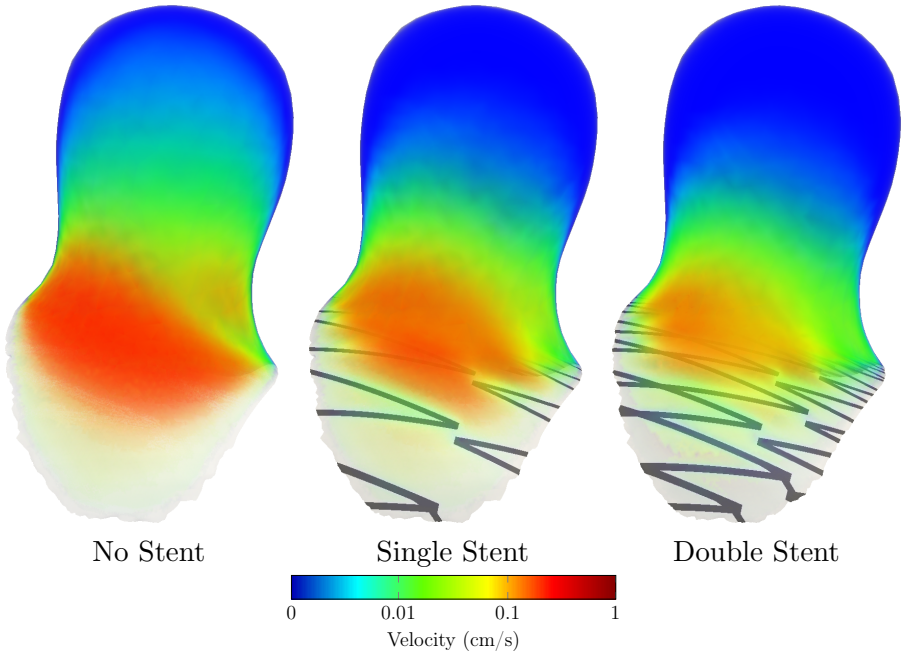

Figure 5.26: Volume rendering of aneurysm velocity magnitude at peak flow into the aneurysm.

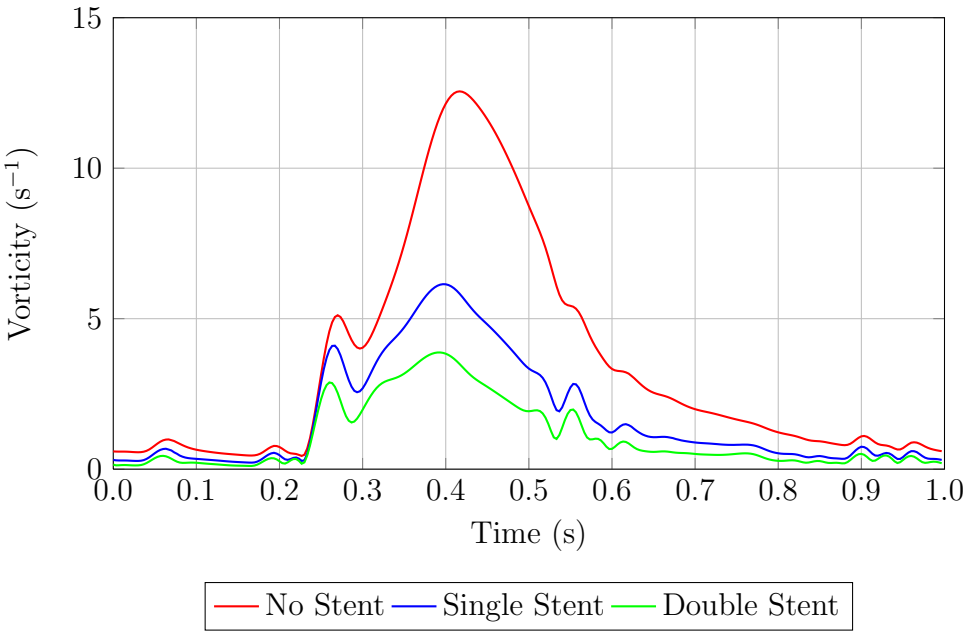

Figure 5.27: Comparison of spatially averaged vorticity magnitude in the aneurysm.

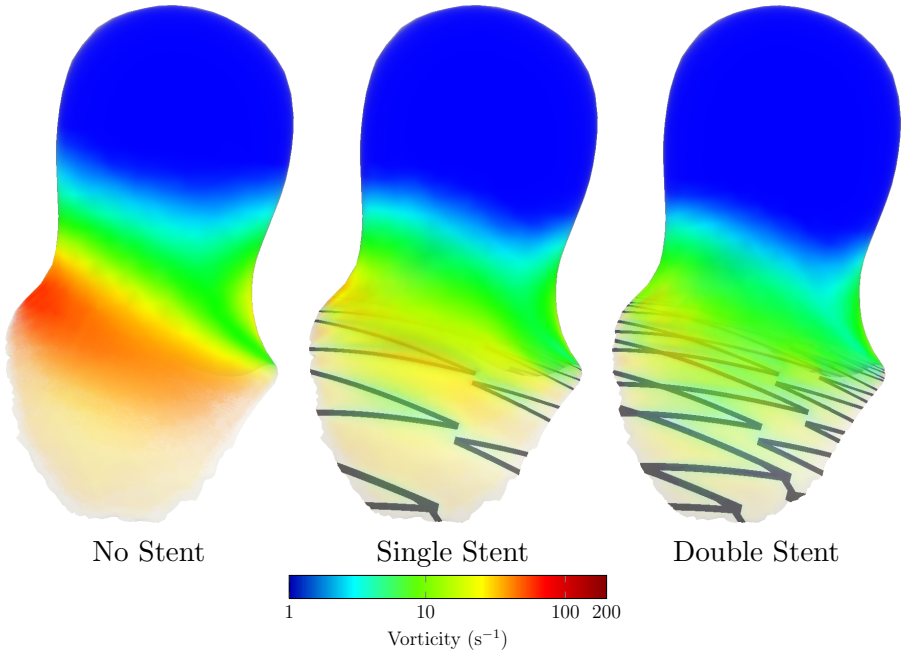

Figure 5.28: Volume rendering of aneurysm vorticity magnitude at peak flow into the aneurysm.

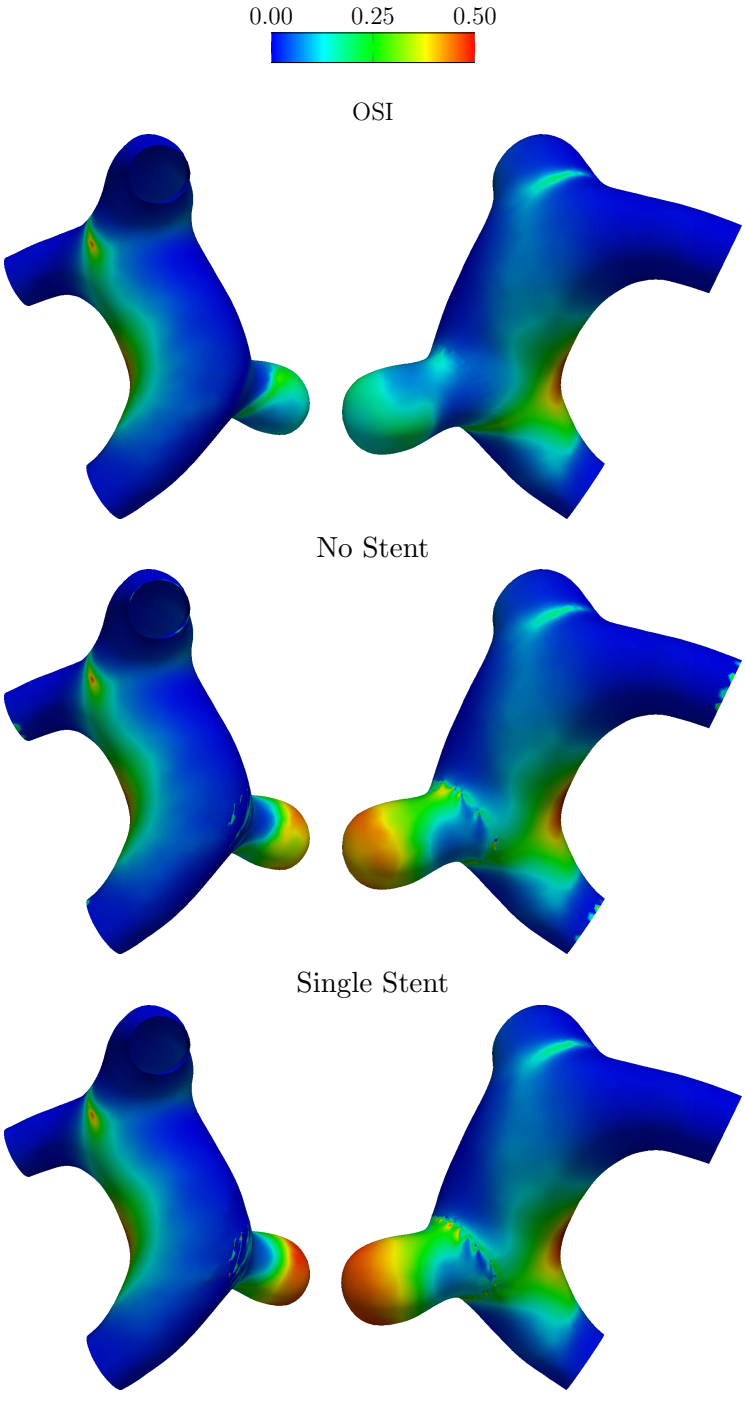

Figure 5.29: OSI for Model 2.

5.2.3 Model 3

The geometry of Model 3 has a pronounced curvature just prior to and at the aneurysm location. The small size of the aneurysm, 0.05 cm^3 in volume, coupled with the significant curvature, results in greater blood flow into and within the aneurysm compared to the other models. The neck of the aneurysm spans an area of 0.60 cm^2, the largest neck area of the four models, contrary to the overall small size of the aneurysm. The single stent covers an area of 0.09 cm^2 and the double stent nearly doubles the area covered to 0.17 cm^2. Figures 5.30–5.33 show the changes induced by deploying a stent to treat the aneurysm. The average inflow rate for the parent artery is slightly higher than the other models at 0.97 ml/s. The peak flow into the aneurysm occurs approximately 0.02 s after peak flow into the parent artery. On average, $\frac{Q_A}{Q_P}$ decreases by 16% and 78% in the single- and double-stent cases, respectively. The single-stent case has a significant drop in average kinetic energy at 66% and the double-stent case is reduced about 87%. The vorticity in the aneurysm follows a similar pattern to kinetic energy and the reduction is shown in Figures 5.34 and 5.35. The average vorticity decreases 41% and 62% in the single- and double-stent cases, respectively. Figure 5.36 shows the OSI for all three cases.

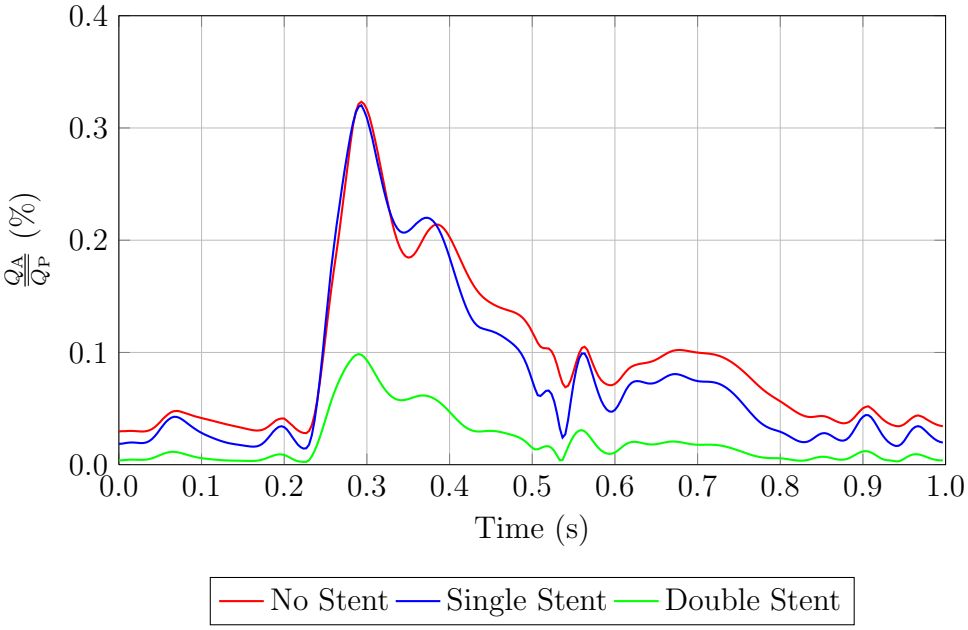

Figure 5.30: Comparison of $\frac{Q_A}{Q_P}$ for the three cases.

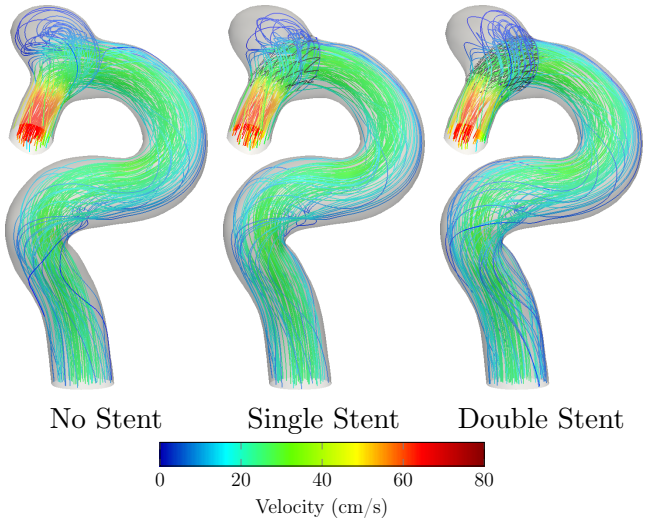

Figure 5.31: Streamlines showing changes in blood flow patterns and velocity induced by stenting at peak flow in the parent artery.

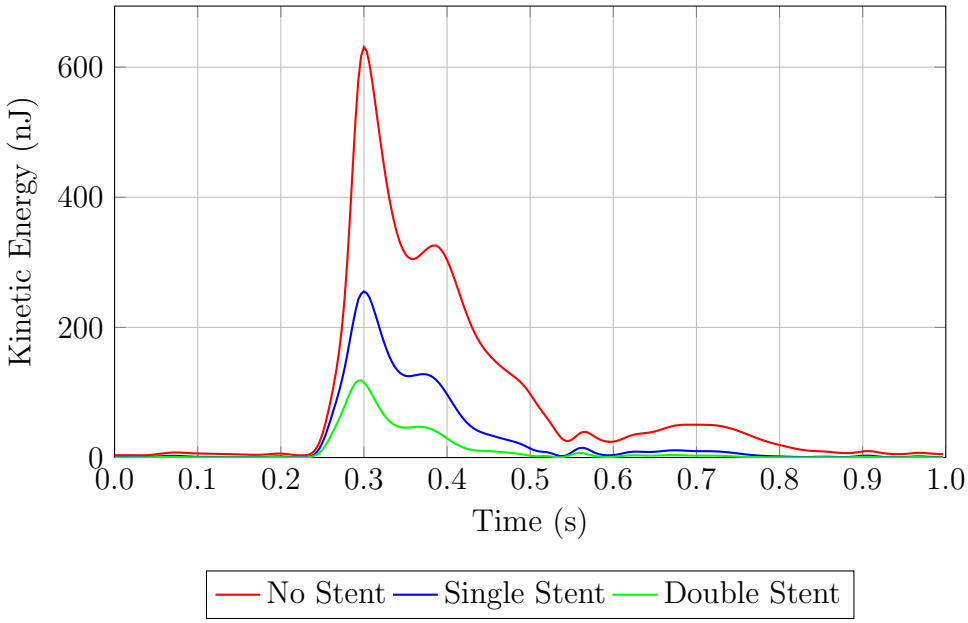

Figure 5.32: Comparison of spatially averaged kinetic energy in the aneurysm.

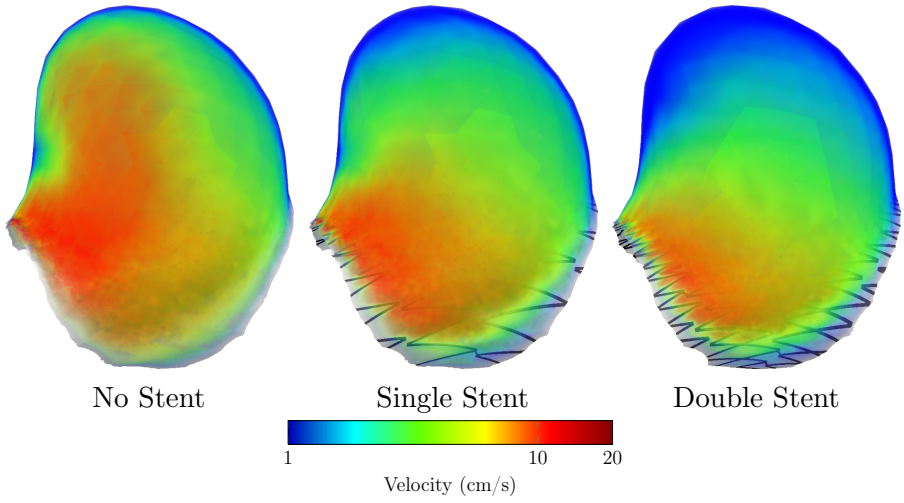

Figure 5.33: Volume rendering of aneurysm velocity magnitude at peak flow into the aneurysm.

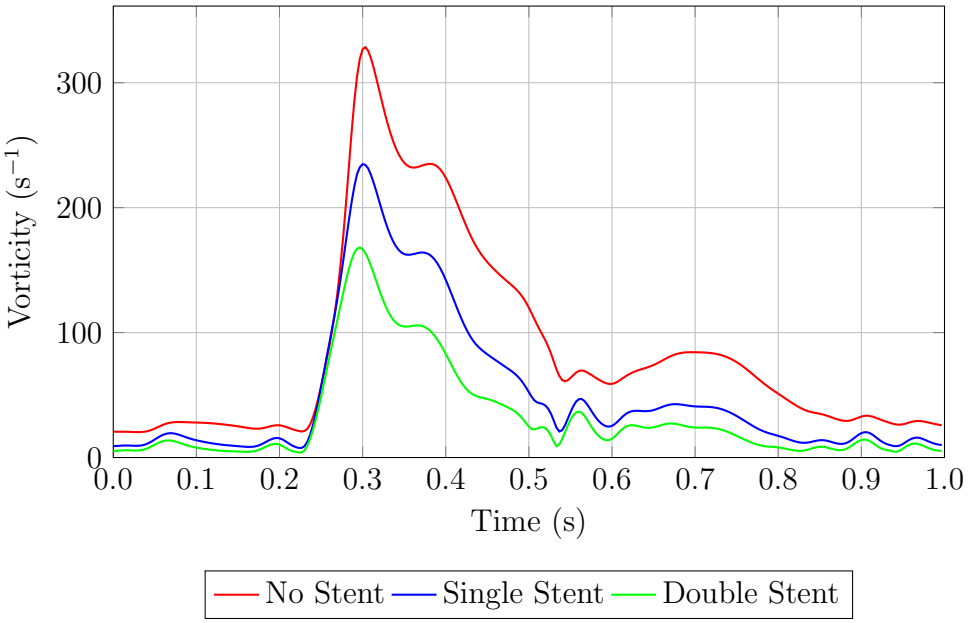

Figure 5.34: Comparison of spatially averaged vorticity magnitude in the aneurysm.

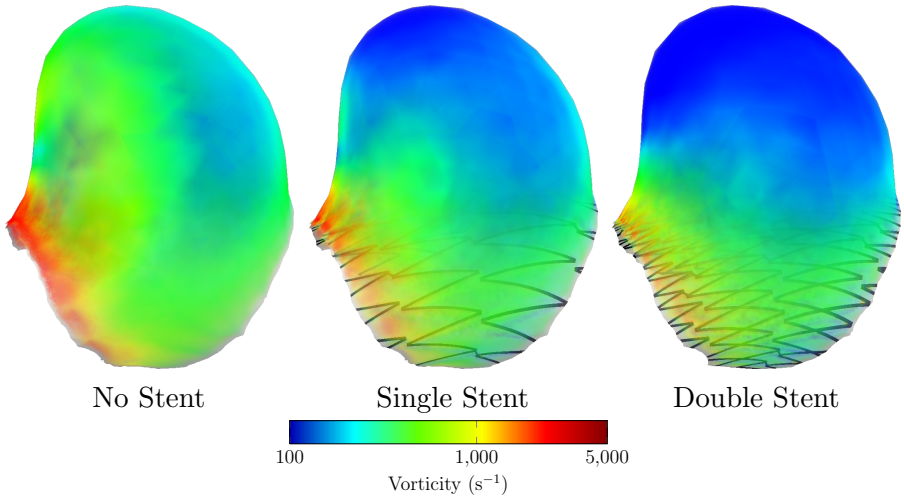

Figure 5.35: Volume rendering of aneurysm vorticity magnitude at peak flow into the aneurysm.

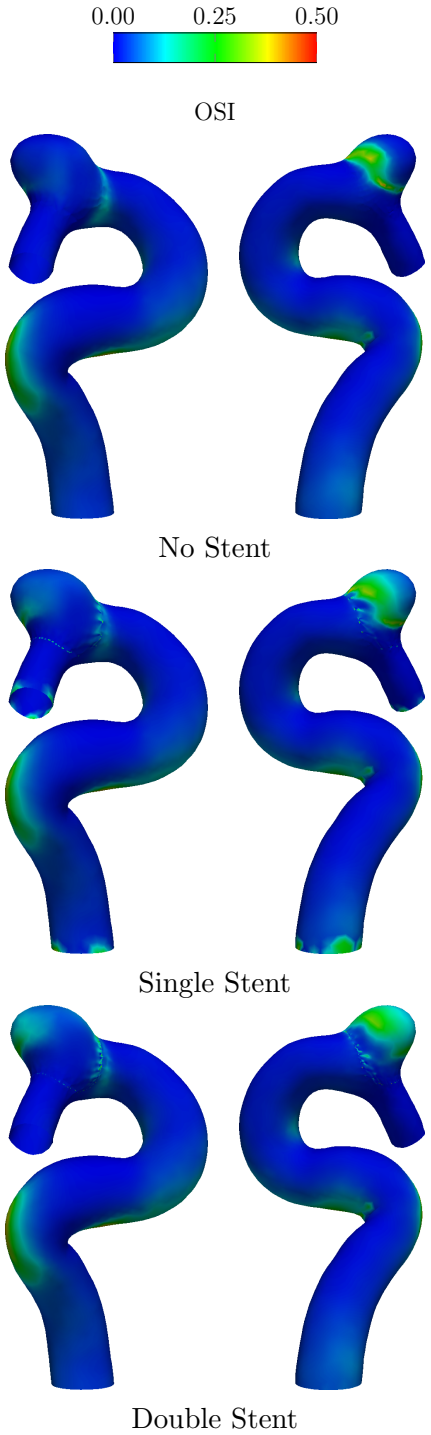

Figure 5.36: OSI for Model 3.

5.2.4 Model 4

Model 4 has the largest aneurysm of the four arteries studied, with a volume of 0.61 cm^3, and has the second largest neck, with an area spanning 0.53 cm^2. The single and double stents cover an area of 0.08 cm^2 and 0.15 cm^2, respectively. A gradual decrease in flow going into the aneurysm is observed from the no-stent case to the double-stent case. The single-stent case has a reduction of 37% in $\frac{Q_A}{Q_P}$ and the double-stent case has a 82% reduction. A dramatic reduction in kinetic energy occurs in both of the stent cases compared to the no-stent case, with 89% decrease in the single-stent case and 97% in the double-stent case. Figures 5.37–5.40 show the reduction in blood flow. The average inflow rate into the parent artery is 0.50 ml/s and the peak blood flow into the aneurysm occurs 0.04 s after peak inflow rate into the parent artery. Similarly to kinetic energy, vorticity drops significantly in the stented cases as shown in Figures 5.41 and 5.42. The average reduction for the single-stent case is 72% and for the double-stent case 86%. The OSI for all three cases is shown in Figure 5.43.

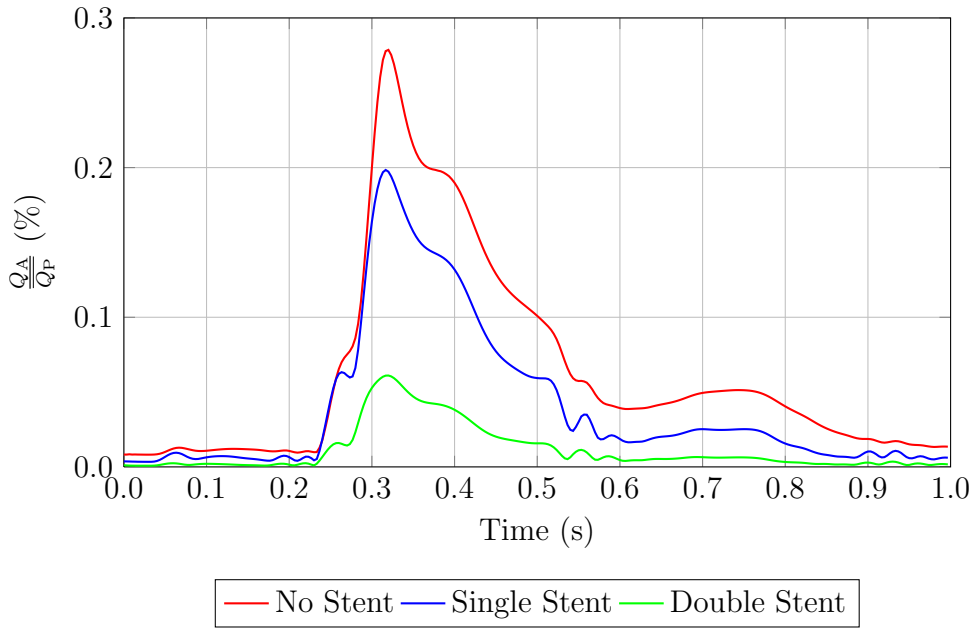

Figure 5.37: Comparison of $\frac{Q_A}{Q_P}$ for the three cases.

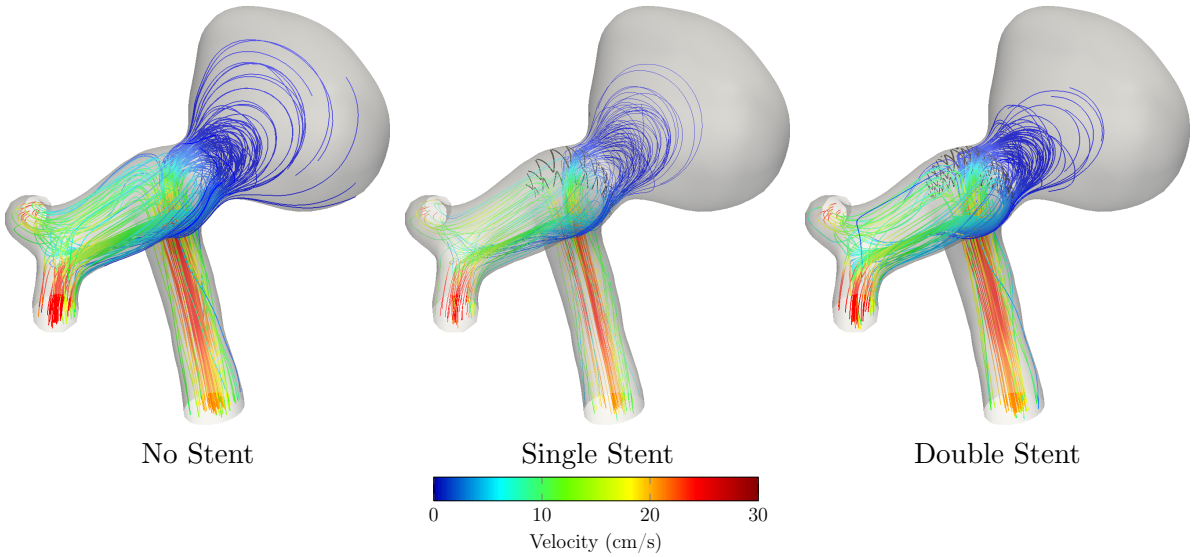

Figure 5.38: Streamlines showing changes in blood flow patterns and velocity induced by stenting at peak flow in the parent artery.

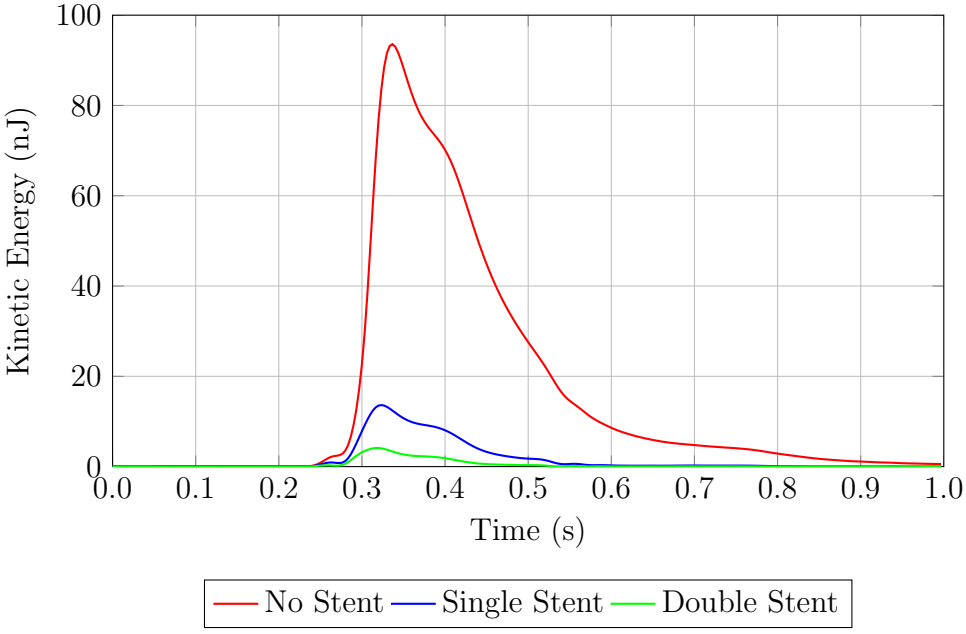

Figure 5.39: Comparison of spatially averaged kinetic energy in the aneurysm.

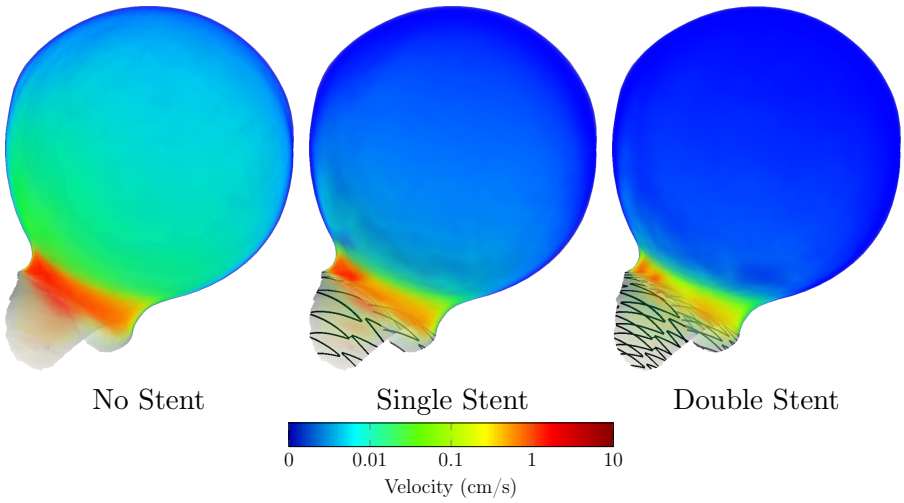

Figure 5.40: Volume rendering of aneurysm velocity magnitude at peak flow into the aneurysm.

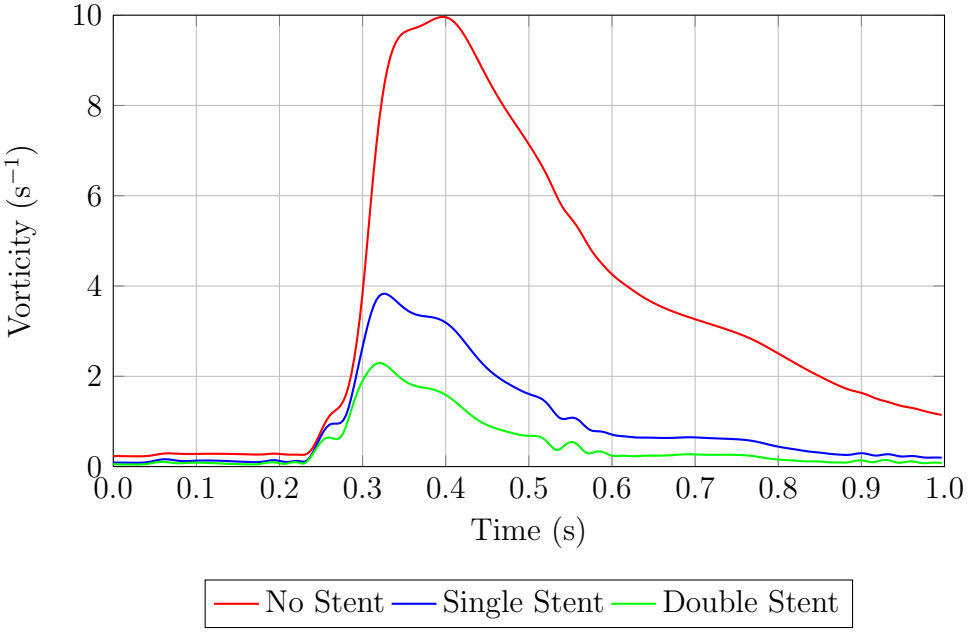

Figure 5.41: Comparison of spatially averaged vorticity magnitude in the aneurysm.

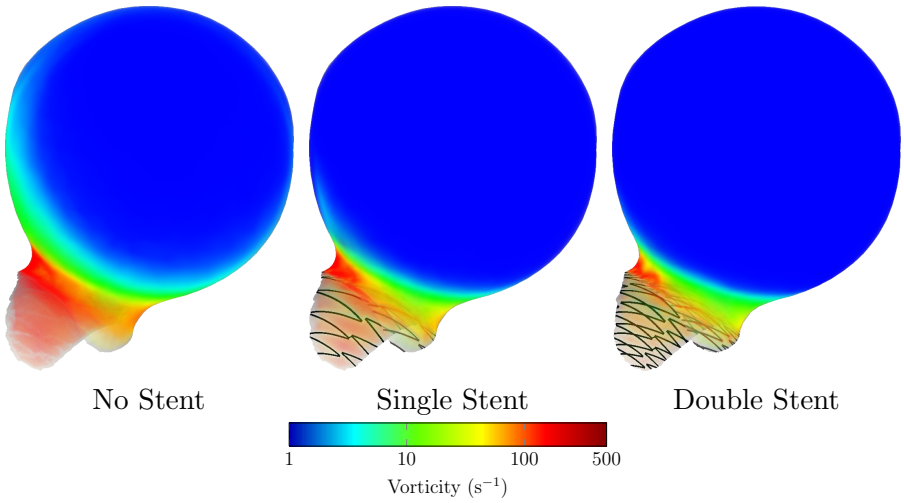

Figure 5.42: Volume rendering of aneurysm vorticity magnitude at peak flow into the aneurysm.

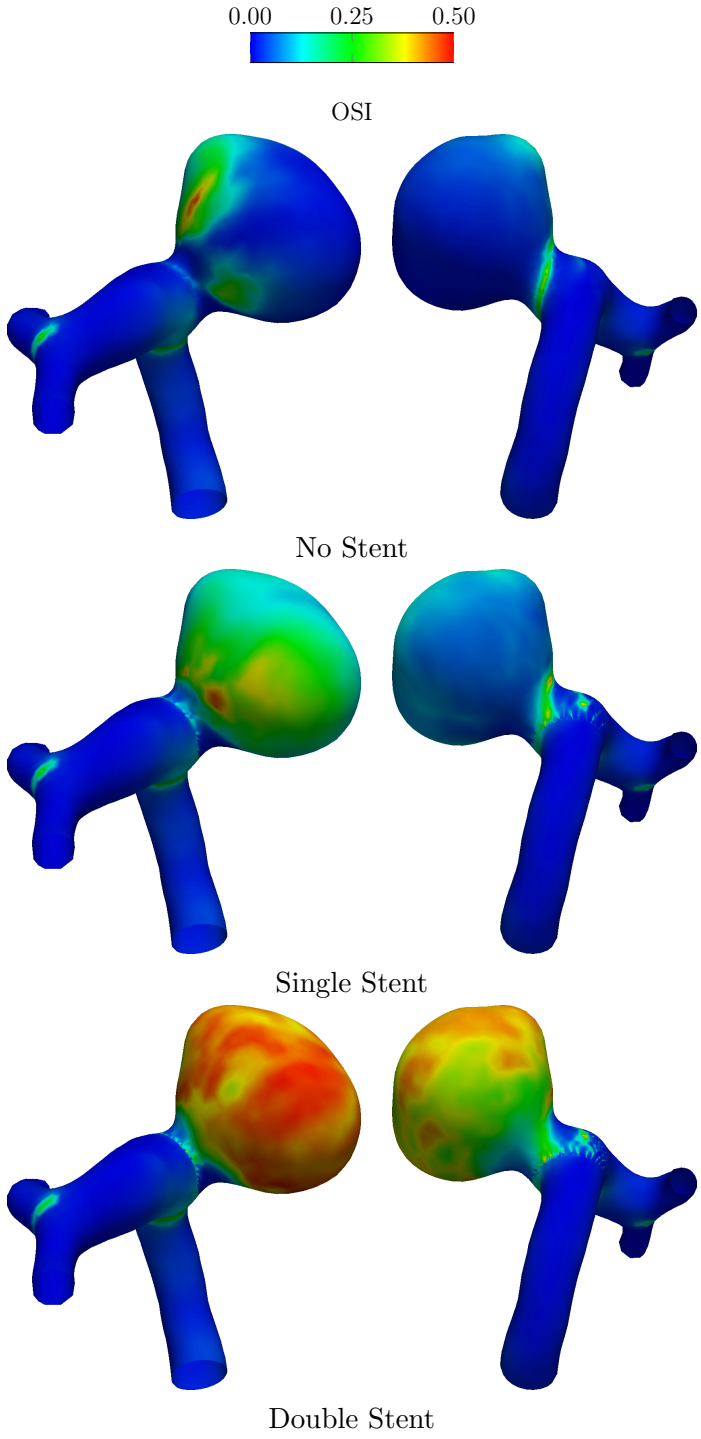

Figure 5.43: OSI for Model 4.

5.3 Evaluation of Zero-Thickness Representation

In modeling the stent, we use a zero-thickness representation, which significantly reduces mesh generation complexity and time required to build the mesh. We compare the zero-thickness representation to a representation with a thickness of approximately 0.01 cm as specified from the Cordis Precise Pro Rx nitinol self-expanding stent. We mesh the finite-thickness representation with 3 to 4 elements across the width of the stent wire and in the thickness direction. Figure 5.44 shows the zero- and finite-thickness representations. Model 1 geometry is used for the comparison of stent representations. Figures 5.45–5.47 and Table 5.4 show, for the zero- and finite-thickness representations, the blood flow in and out of the aneurysm, kinetic energy, and vorticity. Overall, the zero-thickness representation results in a slightly greater flow into and within the aneurysm and slightly more vorticity within the aneurysm than the finite-thickness representation does. On average, the peak values are 9% higher and the average values are 19% higher for the zero-thickness representation. Figure 5.48 shows the comparison of OSI for the zero- and finite-thickness representations of the stent. The spatially-averaged OSI in the aneurysm segment differs by 31.6%, with the zero-thickness representation at 0.27 and the finite-thickness representation at 0.38.

	Average		Peak	
	Zero Thick	Finite Thick	Zero Thick	Finite Thick
$\frac{Q_A}{Q_P}$ (%)	0.022	0.021	0.125	0.129
Kinetic Energy (nJ)	0.53	0.39	6.16	5.43
Vorticity (s^{-1})	4.76	3.84	17.96	17.12

Table 5.4: Average and peak results for the zero- and finite-thickness representations of the stent.

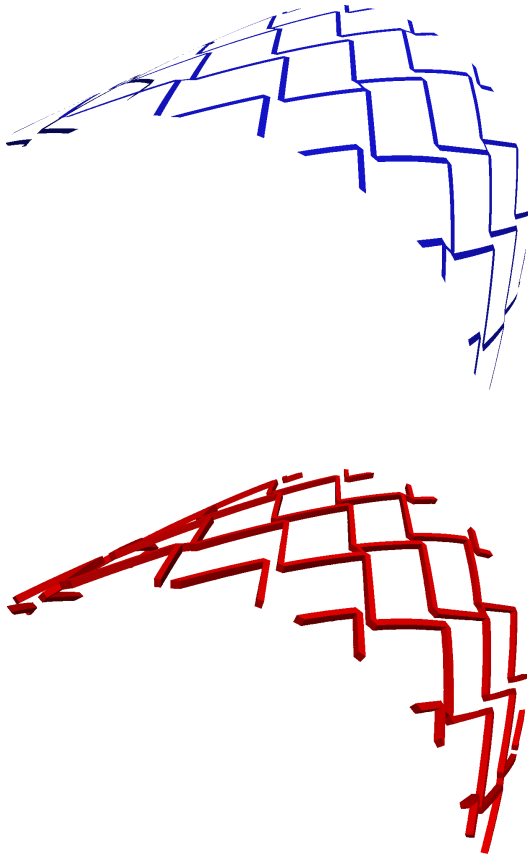

Figure 5.44: Stent surface for zero-thickness (top) and finite-thickness (bottom) representations.

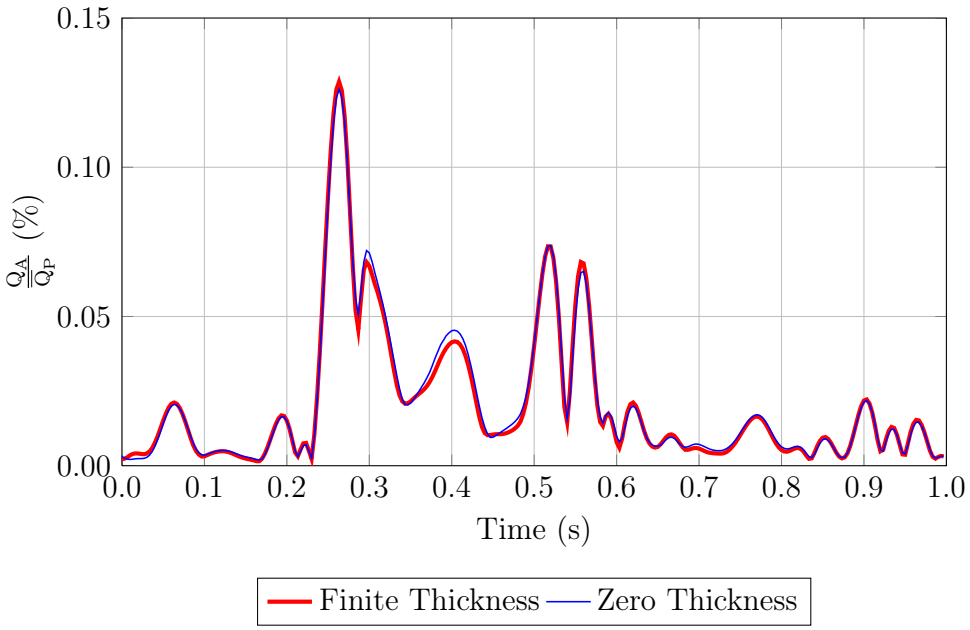

Figure 5.45: Comparison of $\frac{Q_A}{Q_P}$ between zero- and finite-thickness representations of the stent.

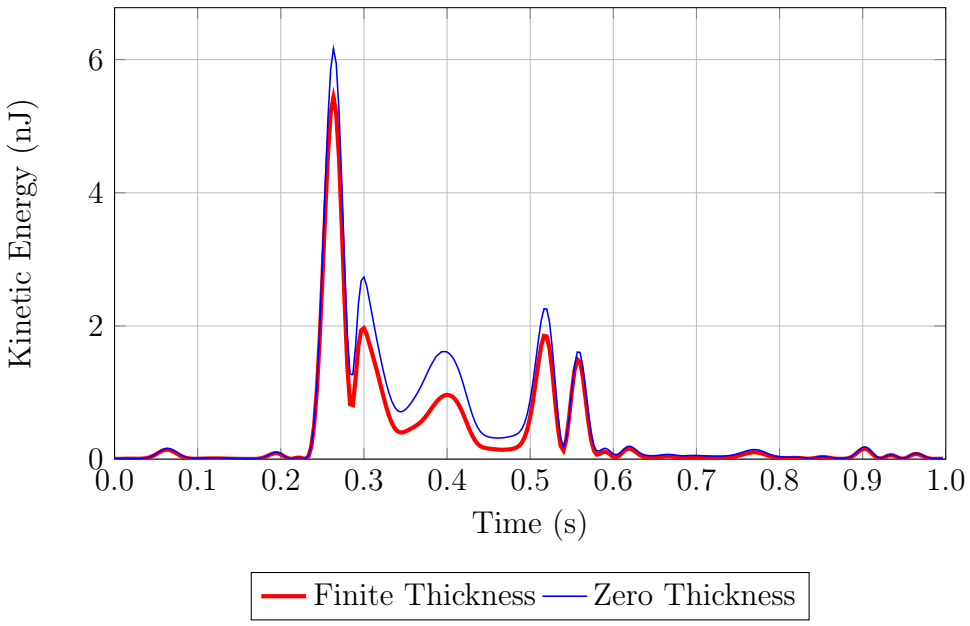

Figure 5.46: Comparison of spatially averaged kinetic energy in the aneurysm between the zero- and finite-thickness representations of the stent.

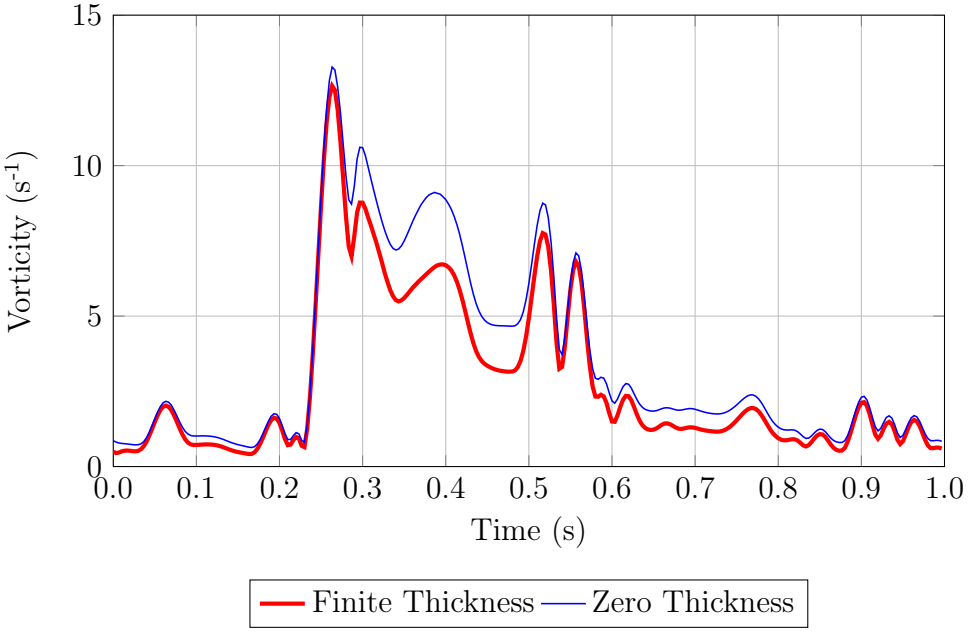

Figure 5.47: Comparison of spatially averaged vorticity magnitude in the aneurysm between the zero- and finite-thickness representations of the stent.

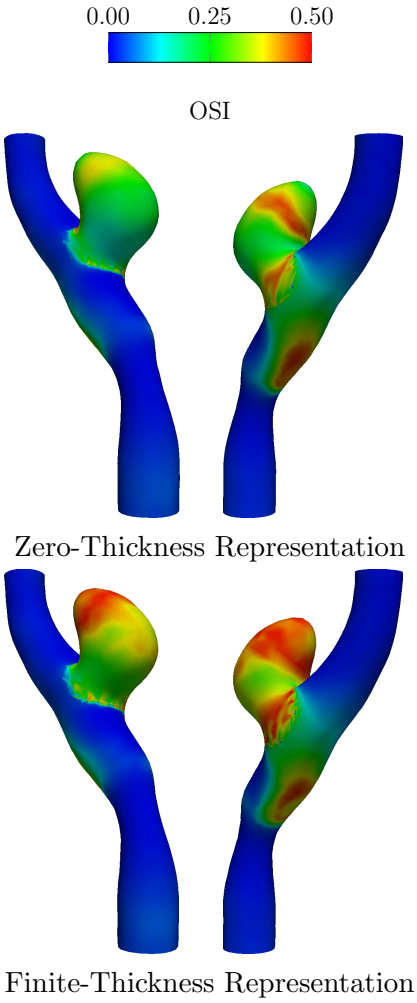

Figure 5.48: OSI for the zero- and finite-thickness representations of the stent.

Chapter 6

Concluding Remarks

The motivation underlying this work was to develop tools and conduct initial studies modeling the hemodynamics in an artery with an aneurysm and stent to further understand the effectiveness of stent treatment. We developed several special techniques including using NURBS for the spatial representation of the surface over which the stent mesh is built, mesh generation techniques for both the finite- and zero-thickness representations of the stent, techniques for generating refined layers of mesh near the arterial and stent surfaces, and models for representing double stent. The techniques were used in conjunction with the DSD/SST-VMST method, which is the core computational technique.

From the study we observe that the flow patterns in the aneurysm are significantly influenced by the presence of single and double stents. The flow rate into and the kinetic energy and vorticity within the aneurysm were all reduced substantially when a single stent was placed across the neck of the aneurysm, and even more when we use a double stent. Additionally, a greater OSI was observed in stented cases. The reduction in blood flow within the aneurysm and increased OSI indicates stagnation of blood flow leading to thrombosis and eventual occlusion of the aneurysm. We also compared the flow patterns obtained with the finite- and zero-thickness representa-

tions of the stent. The computations show that the zero-thickness representation of the stent yields results comparable in peak values to those obtained with the finite-thickness representation. However, the overall average of results differ more between the two representations leading us to think the thickness of the stent may play a more significant role.

Overall, the work presented here provides a comprehensive set of data that we hope will lead to further modeling of cerebral arteries with aneurysm and stent to more completely understand the role stents serve in treating and preventing aneurysm rupture.

Bibliography

[1] Y. Bazilevs and I. Akkerman. Large eddy simulation of turbulent Taylor–Couette flow using isogeometric analysis and the residual–based variational multiscale method. *Journal of Computational Physics*, 229:3402–3414, 2010.

[2] Y. Bazilevs, V. M. Calo, T. J. R. Hughes, and Y. Zhang. Isogeometric fluid–structure interaction: theory, algorithms, and computations. *Computational Mechanics*, 43:3–37, 2008.

[3] Y. Bazilevs, V. M. Calo, T. E. Tezduyar, and T. J. R. Hughes. YZβ discontinuity-capturing for advection-dominated processes with application to arterial drug delivery. *International Journal for Numerical Methods in Fluids*, 54:593–608, 2007.

[4] Y. Bazilevs, V. M. Calo, Y. Zhang, and T. J. R. Hughes. Isogeometric fluid–structure interaction analysis with applications to arterial blood flow. *Computational Mechanics*, 38:310–322, 2006.

[5] Y. Bazilevs, J. C. del Alamo, and J. D. Humphrey. From imaging to prediction: Emerging non-invasive methods in pediatric cardiology. *Progress in Pediatric Cardiology*, 30:81–89, 2010.

[6] Y. Bazilevs, J. R. Gohean, T. J. R. Hughes, R. D. Moser, and Y. Zhang. Patient-specific isogeometric fluid–structure interaction analysis of thoracic aortic blood

flow due to implantation of the Jarvik 2000 left ventricular assist device. *Computer Methods in Applied Mechanics and Engineering*, 198:3534–3550, 2009.

[7] Y. Bazilevs, M.-C. Hsu, D. Benson, S. Sankaran, and A. Marsden. Computational fluid–structure interaction: Methods and application to a total cavopulmonary connection. *Computational Mechanics*, 45:77–89, 2009.

[8] Y. Bazilevs, M.-C. Hsu, Y. Zhang, W. Wang, T. Kvamsdal, S. Hentschel, and J. Isaksen. Computational fluid–structure interaction: Methods and application to cerebral aneurysms. *Biomechanics and Modeling in Mechanobiology*, 9:481–498, 2010.

[9] Y. Bazilevs, M.-C. Hsu, Y. Zhang, W. Wang, X. Liang, T. Kvamsdal, R. Brekken, and J. Isaksen. A fully-coupled fluid–structure interaction simulation of cerebral aneurysms. *Computational Mechanics*, 46:3–16, 2010.

[10] R. L. T. Bevan, P. Nithiarasu, R. V. Loon, I. Sazanov, H. Luckraz, and A. Garnham. Application of a locally conservative Galerkin (LCG) method for modelling blood flow through a patient-specific carotid bifurcation. *International Journal for Numerical Methods in Fluids*, published online, DOI: 10.1002/fld.2313, Mar 2010.

[11] J. R. Cebral, F. Mut, D. Sforza, R. Lohner, E. Scrivano, P. Lylyk, and C. Putnam. Clinical application of image-based cfd for cerebral aneurysms. *International Journal for Numerical Methods in Biomedical Engineering*, published online, DOI: 10.1002/cnm.1373, Mar 2010.

[12] K. Chitra, T. Sundararajan, S. Vengadesan, and P. Nithiarasu. Non-Newtonian blood flow study in a model cavopulmonary vascular system. *International Journal for Numerical Methods in Fluids*, published online, DOI: 10.1002/fld.2256, Mar 2010.

[13] R. Higashida. What you should know about cerebral aneurysms, 2003. `http://avm.ucsf.edu/patient_info/WhatYouShouldKnow/WhatYouShouldKnow.pdf`.

[14] M.-C. Hsu and Y. Bazilevs. Blood vessel tissue prestress modeling for vascular fluid–structure interaction simulations. *Finite Elements in Analysis and Design*, 47:593–599, 2011.

[15] J. G. Isaksen, Y. Bazilevs, T. Kvamsdal, Y. Zhang, J. H. Kaspersen, K. Waterloo, B. Romner, and T. Ingebrigtsen. Determination of wall tension in cerebral artery aneurysms by numerical simulation. *Stroke*, 39:3172–3178, 2008.

[16] L.-D. Jou and M. E. Mawad. Hemodynamic effect of neuroform stent on intimal hyperplasia and thrombus formation in a carotid aneurysm. *Medical Engineering and Physics*, 33(5):573 – 580, 2011.

[17] M. Manguoglu, K. Takizawa, A. H. Sameh, and T. E. Tezduyar. Nested and parallel sparse algorithms for arterial fluid mechanics computations with boundary layer mesh refinement. *International Journal for Numerical Methods in Fluids*, 65:135–149, 2011.

[18] M. Manguoglu, K. Takizawa, A. H. Sameh, and T. E. Tezduyar. A parallel sparse algorithm targeting arterial fluid mechanics computations. *Computational Mechanics*, 48:377–384, 2011.

[19] J. P. Maynard and P. Nithiarasu. A 1D arterial blood flow model incorporating ventricular pressure, aortic valve and regional coronary flow using the locally conservative Galerkin (LCG) method. *Communications in Numerical Methods in Engineering*, 24:367–417, 2008.

[20] F. Mut, R. Aubry, R. Lohner, and J. R. Cebral. Fast numerical solutions of patient-specific blood flows in 3D arterial systems. *International Journal for Numerical Methods in Biomedical Engineering*, 26:73–85, 2010.

[21] L. Pierot. Flow diverter stents in the treatment of intracranial aneurysms: Where are we? *Journal of Neuroradiology*, 38(1):40 – 46, 2011.

[22] K. Rhee, M. Han, S. Cha, and G. Khang. The changes of flow characteristics caused by a stent in fusiform aneurysm models. *Engineering in Medicine and Biology Society, 2001. Proceedings of the 23rd Annual International Conference of the IEEE*, 1:86 – 88, 2001.

[23] V. Roger, A. Go, D. Lloyd-Jones, et. al; American Heart Association Statistics Committee, and S. S. Subcommittee. Heart disease and stroke statistics–2012 update: A report from the american heart association. *Circulation*, 125(1):e78 – e85, 2012.

[24] S. Seshadhri, G. Janiga, O. Beuing, M. Skalej, and D. Thevenin. Impact of stents and flow diverters on hemodynamics in idealized aneurysm models. *Journal of Biomechanical Engineering*, 133(7):1 – 9, 2011.

[25] K. Sugiyama, S. Ii, S. Takeuchi, S. Takagi, and Y. Matsumoto. Full Eulerian simulations of biconcave neo-Hookean particles in a Poiseuille flow. *Computational Mechanics*, 46:147–157, 2010.

[26] K. Takizawa, Y. Bazilevs, and T. E. Tezduyar. Space–time and ALE-VMS techniques for patient-specific cardiovascular fluid–structure interaction modeling. *Archives of Computational Methods in Engineering*, to appear, 2012.

[27] K. Takizawa, T. Brummer, T. E. Tezduyar, and P. R. Chen. A comparative study based on patient-specific fluid–structure interaction modeling of cerebral aneurysms. *Journal of Applied Mechanics*, 79:010908, 2012.

[28] K. Takizawa, J. Christopher, T. E. Tezduyar, and S. Sathe. Space–time finite element computation of arterial fluid–structure interactions with patient-specific

data. *International Journal for Numerical Methods in Biomedical Engineering*, 26:101–116, 2010.

[29] K. Takizawa, B. Henicke, A. Puntel, T. Spielman, and T. E. Tezduyar. Space–time computational techniques for the aerodynamics of flapping wings. *Journal of Applied Mechanics*, 79:010903, 2012.

[30] K. Takizawa, C. Moorman, S. Wright, J. Christopher, and T. E. Tezduyar. Wall shear stress calculations in space–time finite element computation of arterial fluid–structure interactions. *Computational Mechanics*, 46:31–41, 2010.

[31] K. Takizawa, C. Moorman, S. Wright, J. Purdue, T. McPhail, P. R. Chen, J. Warren, and T. E. Tezduyar. Patient-specific arterial fluid–structure interaction modeling of cerebral aneurysms. *International Journal for Numerical Methods in Fluids*, 65:308–323, 2011.

[32] K. Takizawa and T. E. Tezduyar. Multiscale space–time fluid–structure interaction techniques. *Computational Mechanics*, 48:247–267, 2011.

[33] K. Takizawa and T. E. Tezduyar. Space–time fluid–structure interaction methods. *Mathematical Models and Methods in Applied Sciences*, to appear, 2012.

[34] T. E. Tezduyar. Stabilized finite element formulations for incompressible flow computations. *Advances in Applied Mechanics*, 28:1–44, 1992.

[35] T. E. Tezduyar. Computation of moving boundaries and interfaces and stabilization parameters. *International Journal for Numerical Methods in Fluids*, 43:555–575, 2003.

[36] T. E. Tezduyar, M. Behr, and J. Liou. A new strategy for finite element computations involving moving boundaries and interfaces – the deforming-spatial-domain/space–time procedure: I. The concept and the preliminary numerical

tests. *Computer Methods in Applied Mechanics and Engineering*, 94(3):339–351, 1992.

[37] T. E. Tezduyar, M. Behr, S. Mittal, and J. Liou. A new strategy for finite element computations involving moving boundaries and interfaces – the deforming-spatial-domain/space–time procedure: II. Computation of free-surface flows, two-liquid flows, and flows with drifting cylinders. *Computer Methods in Applied Mechanics and Engineering*, 94(3):353–371, 1992.

[38] T. E. Tezduyar, T. Cragin, S. Sathe, and B. Nanna. FSI computations in arterial fluid mechanics with estimated zero-pressure arterial geometry. In E. Onate, J. Garcia, P. Bergan, and T. Kvamsdal, editors, *Marine 2007*, Barcelona, Spain, 2007. CIMNE.

[39] T. E. Tezduyar and S. Sathe. Modeling of fluid–structure interactions with the space–time finite elements: Solution techniques. *International Journal for Numerical Methods in Fluids*, 54:855–900, 2007.

[40] T. E. Tezduyar, S. Sathe, T. Cragin, B. Nanna, B. S. Conklin, J. Pausewang, and M. Schwaab. Modeling of fluid–structure interactions with the space–time finite elements: Arterial fluid mechanics. *International Journal for Numerical Methods in Fluids*, 54:901–922, 2007.

[41] T. E. Tezduyar, S. Sathe, M. Schwaab, and B. S. Conklin. Arterial fluid mechanics modeling with the stabilized space–time fluid–structure interaction technique. *International Journal for Numerical Methods in Fluids*, 57:601–629, 2008.

[42] T. E. Tezduyar, M. Schwaab, and S. Sathe. Sequentially-Coupled Arterial Fluid–Structure Interaction (SCAFSI) technique. *Computer Methods in Applied Mechanics and Engineering*, 198:3524–3533, 2009.

[43] T. E. Tezduyar, K. Takizawa, T. Brummer, and P. R. Chen. Space–time fluid–structure interaction modeling of patient-specific cerebral aneurysms. *International Journal for Numerical Methods in Biomedical Engineering*, 27:1665–1710, 2011.

[44] T. E. Tezduyar, K. Takizawa, and J. Christopher. Multiscale Sequentially-Coupled Arterial Fluid–Structure Interaction (SCAFSI) technique. In S. Hartmann, A. Meister, M. Schaefer, and S. Turek, editors, *International Workshop on Fluid–Structure Interaction — Theory, Numerics and Applications*, pages 231–252. Kassel University Press, 2009.

[45] T. E. Tezduyar, K. Takizawa, C. Moorman, S. Wright, and J. Christopher. Multiscale sequentially-coupled arterial FSI technique. *Computational Mechanics*, 46:17–29, 2010.

[46] R. Torii, M. Oshima, T. Kobayashi, K. Takagi, and T. E. Tezduyar. Influence of wall elasticity on image-based blood flow simulation. *Japan Society of Mechanical Engineers Journal Series A*, 70:1224–1231, 2004. in Japanese.

[47] R. Torii, M. Oshima, T. Kobayashi, K. Takagi, and T. E. Tezduyar. Computer modeling of cardiovascular fluid–structure interactions with the Deforming-Spatial-Domain/Stabilized Space–Time formulation. *Computer Methods in Applied Mechanics and Engineering*, 195:1885–1895, 2006.

[48] R. Torii, M. Oshima, T. Kobayashi, K. Takagi, and T. E. Tezduyar. Fluid–structure interaction modeling of aneurysmal conditions with high and normal blood pressures. *Computational Mechanics*, 38:482–490, 2006.

[49] R. Torii, M. Oshima, T. Kobayashi, K. Takagi, and T. E. Tezduyar. Influence of wall elasticity in patient-specific hemodynamic simulations. *Computers & Fluids*, 36:160–168, 2007.

[50] R. Torii, M. Oshima, T. Kobayashi, K. Takagi, and T. E. Tezduyar. Numerical investigation of the effect of hypertensive blood pressure on cerebral aneurysm — Dependence of the effect on the aneurysm shape. *International Journal for Numerical Methods in Fluids*, 54:995–1009, 2007.

[51] R. Torii, M. Oshima, T. Kobayashi, K. Takagi, and T. E. Tezduyar. Fluid–structure interaction modeling of a patient-specific cerebral aneurysm: Influence of structural modeling. *Computational Mechanics*, 43:151–159, 2008.

[52] R. Torii, M. Oshima, T. Kobayashi, K. Takagi, and T. E. Tezduyar. Fluid–structure interaction modeling of blood flow and cerebral aneurysm: Significance of artery and aneurysm shapes. *Computer Methods in Applied Mechanics and Engineering*, 198:3613–3621, 2009.

[53] R. Torii, M. Oshima, T. Kobayashi, K. Takagi, and T. E. Tezduyar. Influence of wall thickness on fluid–structure interaction computations of cerebral aneurysms. *International Journal for Numerical Methods in Biomedical Engineering*, 26:336–347, 2010.

[54] R. Torii, M. Oshima, T. Kobayashi, K. Takagi, and T. E. Tezduyar. Role of 0D peripheral vasculature model in fluid–structure interaction modeling of aneurysms. *Computational Mechanics*, 46:43–52, 2010.

[55] R. Torii, M. Oshima, T. Kobayashi, K. Takagi, and T. E. Tezduyar. Influencing factors in image-based fluid–structure interaction computation of cerebral aneurysms. *International Journal for Numerical Methods in Fluids*, 65:324–340, 2011.

[56] R. E. Wells Jr. and E. W. Merrill. Shear rate dependence of the viscosity of whole blood and plasma. *Science*, 133(3455):763–764, 1961.

[57] J. R. Womersley. Method for the calculation of velocity, rate of flow and viscous drag in arteries when the pressure gradient is known. *Journal of Physiology*, 127:553–563, 1955.

[58] G. K. Wong, H.-B. Tan, M. C. Kwan, R. Y. Ng, S. C. Yu, X.-L. Zhu, and W.-S. Poon. Evolution of intracranial aneurysm treatment: From hunterian ligation to the flow diverter. *Surgical Practice*, 15(1):16 – 20, 2011.